

ENERGY TRANSFER PATHWAYS FOR NO₂-RARE GAS
COMPLEXES IN HELIUM NANODROPLETS

by

Anton Zadorozhnyy

Contents

I. Introduction	1
II. Helium nanodroplet experiment	5
Helium Droplet Isolation Technique	5
Production of droplet beams	7
Capture of foreign species	10
Mass Depletion Spectroscopy	13
Helium Droplet Machine	16
References and notes	23
III. Visible spectroscopy of NO₂ in helium droplets	24
Electronic Spectroscopy in Helium Droplets	24
Shifts	29
Theoretical model	35
References and notes	42
IV. Adding rare gas atoms to helium droplets doped with NO₂	45
Capture and ionization of rare gas atoms within helium droplets	45
Calibration of the pickup cell pressure variation technique	54
References and notes	63
V. Experimental results	65
Extension of the mass depletion spectrum to the region of 17350–17750 cm ⁻¹	65
Visible spectroscopy of NO ₂ -rare gas complexes in helium droplets	70
Results	70
Discussion	75
References and notes	84
VI. Future work	85
Appendix A	88

I. Introduction

For more than a decade [1] helium droplet isolation spectroscopy has been recognized as versatile technique for studying the properties of atomic and molecular systems. Using helium droplets as a solvent allowed to overcome numerous difficulties of embedding foreign species into bulk liquid helium. The ability of droplets to capture anything on their path, first demonstrated by Toennies and co-workers in 1990 [2], opened up the pathways for spectroscopic investigations of atoms and molecules of virtually any kind. Unique properties of He droplets, such as evaporative cooling down to 0.37 K and superfluidity, make them both an ideal isolation host material and an interesting research subject in itself.

Explored in this thesis are the properties of one of the components of microsolvation in helium: namely, the locally non-superfluid shell of atoms that encrusts the embedded species. Nitrogen dioxide, NO_2 , was chosen as a probe molecule for it had been studied extensively in the gas phase [4]. It also represents a textbook example of the regime of vibronic chaos when photoexcited to the region above the conical intersection between its two lowest electronic states X^2A_1 and A^2B_2 [5]. Previous experiments with NO_2 -doped helium droplets [6, 7] revealed small homogeneous perturbations of the gas-phase spectral features. This suggested that the intramolecular dynamics of the dopant can be qualitatively separated from that of the host in a fashion similar to the Born-Oppenheimer approximation due to the chaotic nature of

NO₂ vibrations and vast difference in characteristic timescales. In the same time, fast relaxation showed that the non-superfluid shell around NO₂ is the primary mediator of the energy transfer between the excited molecule and the helium bath. Experiments described in this work aim to further characterize this shell by co-embedding the nitrogen dioxide with atoms of rare gases, thus changing its structure and dynamics in a systematic manner. The motivation for these experiments comes from previous unsuccessful attempts, where it has been prematurely reported that addition “*even a single Ne atom obliterated the [spectral] structure...*” [6] The major result of this work is the substantial understanding and refinement of the rare gas pickup process. Through careful calibration of the gas-dosing and monitoring functions of the experimental apparatus it was possible to successively embed one, two and three rare gas atoms on average. This led to observation of a gradual effect induced by rare gas atoms on the spectral features of NO₂ in helium droplets.

The material in this thesis is organized as follows. Chapter II begins with the introduction of the helium droplet isolation technique, and then discusses the practical aspects of droplet beams production, characterization, and principles of mass depletion spectroscopy. Helium droplet apparatus used in this work is also described in this chapter. Chapter III provides an overview of the previous results of mass depletion spectroscopy of NO₂ molecule in helium droplets. This is followed by the theoretical model for the mechanisms responsible for the observed helium-induced shifts and broadening of the spectral lines. Capture and ionization of rare gas atoms in helium droplets are

considered in detail in Chapter IV. This chapter also describes the calibration of the pickup cell pressure variation technique, which allowed for controlled doping of droplets by desired number of rare gas atoms on average. Chapter V contains the experimental results of this work. These results include the extension of previously obtained spectrum of NO₂ in helium droplets to the region of lower excitation energies, and the mass depletion spectroscopy of NO₂·RG complexes in helium droplets, where RG = Ne, Ar, Kr and Xe. For the latter set of experiments, only addition of neon resulted in an observable effect on the spectral features. This effect, as well as its absence in the case of other rare gases, is discussed in terms of the proposed model and the qualitative differences between different rare gases. Finally, Chapter VI outlines some possible directions for future research on this subject.

References and notes

1. K. K. Lehmann, G. Scoles, *Science* 279, 2065 (1998)
2. A. Scheidemann, B. Schilling, J. P. Toennies, J. A. Northby, *Physica B* 165, 135 (1990)
3. F. Paesani, F. A. Gianturco, K. B. Whaley, *Europhys. Lett.* 56, 658 (2001)
4. a) C. G. Stevens, M. W. Swagel, R. Wallace, R. N. Zare, *Chem. Phys. Lett.* 18(4), 465 (1973); b) A. Delon, R. Georges, R. Jost, *J. Chem. Phys.* 103(18), 7740 (1995) and references therein
5. R. Georges, A. Delon, R. Jost, *J. Chem. Phys.* 103(5), 1732 (1995)
6. E. Polyakova, D. Stolyarov, X. Zhang, V. V. Kresin, C. Wittig, *Chem. Phys. Lett.* 375(3-4), 253 (2003)
7. D. Stolyarov, E. Polyakova, C. Wittig, *J. Phys. Chem. A* 108(45), 9841 (2004)

II. Helium Nanodroplet Experiment

Helium Droplet Isolation Technique

Obtaining detailed energetic and structural information about molecular species is the primary subject of high-resolution spectroscopy. Experimental methods in this field ultimately require the isolation of a single molecule to avoid dealing with complex effects of the surrounding medium. In addition, a well-defined initial state is needed for most spectroscopic studies – a molecule has to be cooled down as close to the ground state as possible. Seeded molecular beams [1] and gas crystal matrix isolation [2] have been used extensively to achieve these conditions. However, both of these methods have fundamental limitations. Although significant cooling can be achieved via collisions during the expansion, hot bands may still complicate the spectra obtained from molecular beams. Furthermore, employing this method to study clusters and complexes is troublesome because of the lack of control available over cluster sizes and compositions.

Freezing molecular species in crystalline matrices of rare gases or hydrogen allows for cooling to sub-Kelvin temperatures ($T \leq 1$ K) [2]. The major limitation of matrix isolation is the strong interaction of embedded molecules with the host

structure, which leads to considerable inhomogeneous broadening of the spectral lines [3].

Using helium as a matrix host material eliminates this broadening. Large quantum mechanical delocalization makes it the only substance that remains liquid at zero Kelvin. Additionally, this unique characteristic allows helium environment to adapt itself to accommodate the impurity without perturbation. Another advantage of helium matrix isolation is that it is completely transparent to radiation in wide spectral range: from far IR to VUV. The most fascinating property of liquid ^4He is that below 2.2 K it undergoes a unique phase transition to the superfluid state [4]. In this state, helium environment allows embedded molecules to move freely. However, the constant challenge of immersing foreign species into the bath of helium imposes a significant limitation on a number of species that can be studied. Only experiments with metal atoms, small clusters and ions have been reported so far [5].

Helium droplet beam technique has established itself as a powerful tool in the arsenal of a modern spectroscopist [5-9]. It is in essence a marriage of seeded molecular beams and gas crystal matrix isolation. Helium droplets solve the problem of cooling, while providing a benign host environment for an embedded molecule. The preparation of droplet beams is a straightforward procedure, involving commercially available equipment, and there are no restrictions on the type of species that can be isolated inside or on the surface of a droplet.

Additionally, each droplet can be viewed as a “personal” nano-cryostat that keeps the embedded molecule at 0.37 K – the excess energy is dissipated by quantum evaporation of helium atoms from the surface, with each atom requiring about 5 cm^{-1} (for the most commonly studied droplets of 10^4 atoms). The rest of this section provides the details on production, characteristics and doping of the helium droplet beams.

Production of droplet beams

The formation of helium droplets as a result of adiabatic change in state has been observed as early as 1908 by Kamerlingh Onnes during his attempts to liquefy helium [10]. The first beams of helium droplets were produced by Becker and co-workers in 1961 [11]. Today helium droplet beams are easily generated by expansion of helium through a small nozzle in three qualitatively different regimes, classified by the initial conditions of expansion:

- *sub-critical*, whereupon the gaseous helium is expanded and the expansion isentrope approaches the evaporation line from below the critical point (for ${}^4\text{He}$, $T_c = 5.2 \text{ K}$, $P_c = 2.27 \text{ bar}$) on the phase diagram, Figure 2-1; droplets of $\bar{N} < 5 \cdot 10^4$ atoms are produced

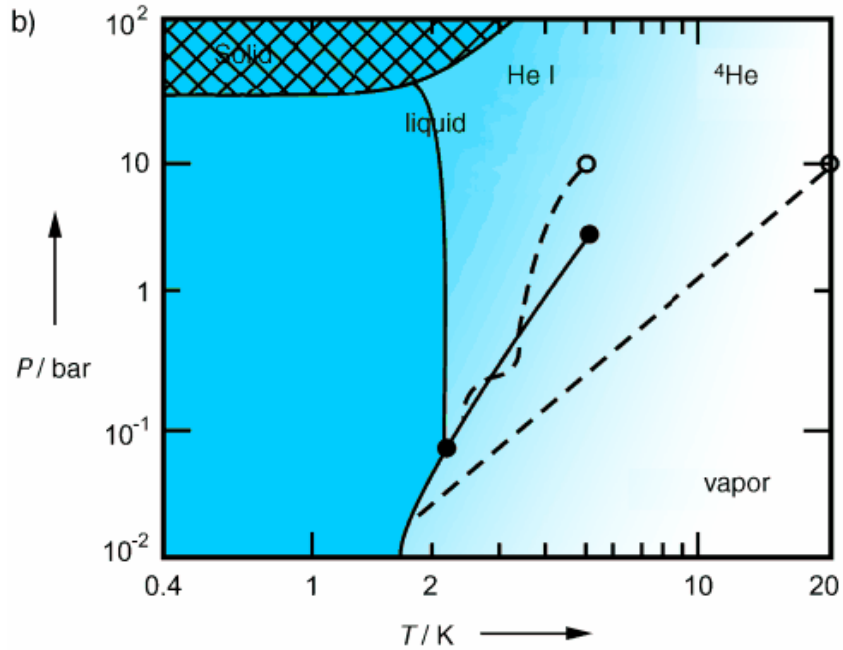


Figure 2-1. Phase diagram of helium. Dashed lines represent expansion isentropes [6]

- *critical*, when the expansion occurs along the evaporation line
- *supercritical*, in which the helium liquid is expanded; this regime is characterized by the formation of large droplets with $\bar{N} > 10^6$ atoms

Droplet beams produced in the sub-critical regime are the most widely used and have been studied in detail [12]. Following the expansion, the temperature and pressure of helium decreases rapidly, leading to condensation and

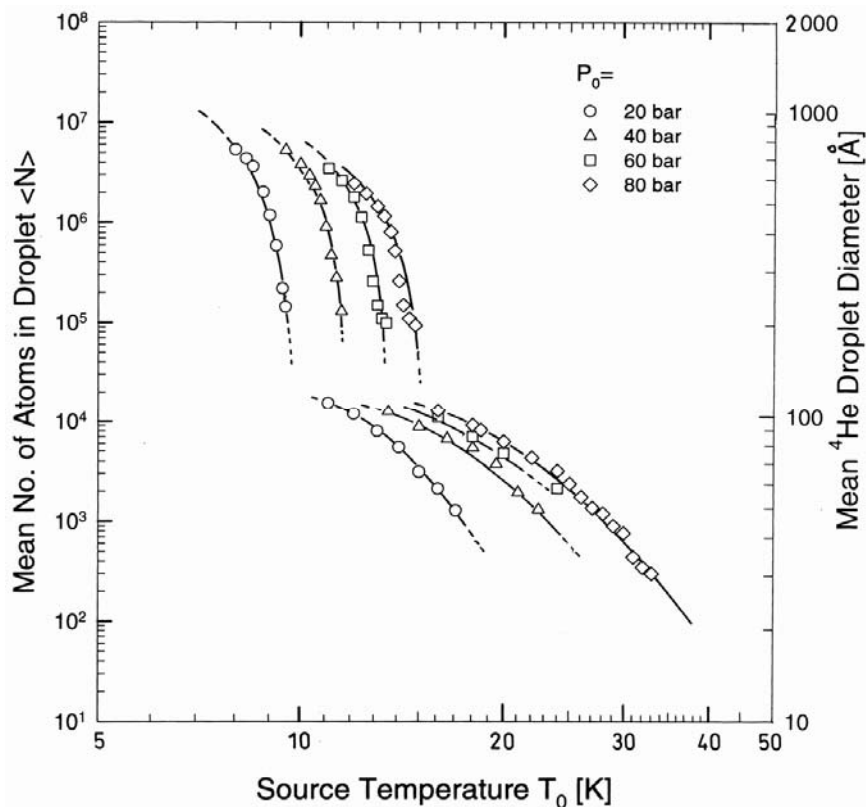


Figure 2-2. Measured mean number of atoms in ^4He droplets as a function of source temperature [17]

consequent clusterization. At distances of about 1000 orifice diameter from the nozzle, the collisions gradually subside and the droplets are further cooled by evaporation, reaching the equilibrium temperature of 0.37 K. This temperature is dictated by unique thermodynamics and structure of helium droplets, which have been studied in detail [13-16].

The distribution of droplets sizes in the beam follows a log-normal form and is determined by the temperature and pressure conditions of the nozzle. Figure 2-2

shows the average droplet size dependence on these parameters [17], as obtained from scattering experiments. The droplet diameter can be estimated using the liquid drop model, in which droplets are assumed spherical and having a density of bulk liquid helium: $D = 2.22N^{1/3} \text{ \AA}$ (for ^4He) [7]. The mean velocity of the droplets in the beam depends on the temperature of the nozzle and varies from 250 – 450 m/s for temperatures from 10 – 20 K, respectively. Hence, for the characteristic length of an experimental apparatus of about 1 m, the lifetime of a droplet is about 3 ms.

Capture of foreign species

The ability of helium droplets to pick up any species with which they collide has been demonstrated by early experiments in Toennies' group [18]. The pickup is accomplished by passing the droplet beam through a pickup cell, which is filled with the gas of molecules to be embedded. For low-vapor-pressure species, such as metals or large organic molecules, vaporization techniques vary, although typically these species are sublimed in a heated cell. The embedded molecule deposits its kinetic and internal energy, as well as its chemical potential, into the droplet. This leads to evaporation of helium atoms and a subsequent decrease of the droplet size. For droplets consisting of about 10^4 atoms, the pickup of a molecule such as SF_6 leads to the loss of about 600 atoms [19]. If the loss of helium atoms is neglected and the pickup cross-section is assumed to be the same for each consecutive collision, the probability to pickup k molecules is given by the Poisson distribution:

$$I_k = I_0 \frac{\left(\frac{P}{k_B T} \sigma L\right)^k}{k!} \exp\left(-\frac{P}{k_B T} \sigma L\right),$$

where σ is the pickup cross-section, L is the length of the pickup cell, P and T are temperature and pressure of the gas in the cell, respectively. For a typical pickup cell with a length ~ 5 cm, pressures on the order of $10^{-5} - 10^{-6}$ mbar are needed to pickup 1-2 molecules on average. Within the droplet, molecules are expected to move freely and coagulate into sub-clusters [19]. The composition and structure of these sub-clusters may be controlled by passing the droplet beam through a series of different pickup cells [20].

Location of atoms and molecules in the helium droplet depends on the interaction of these species with helium. A model developed by Ancilotto et al. [21] introduces a dimensionless parameter λ , which is used to determine the preferred position of a particular dopant:

$$\lambda = 2^{-1/6} \frac{\rho \varepsilon r_e}{\sigma},$$

where ρ is the density and σ is the surface tension of liquid helium, ε is depth and r_e is the equilibrium distance for the impurity-helium pair potential. When $\lambda < 1.9$ it is more energetically favorable for an impurity to reside on the surface, while dopants for which $\lambda > 1.9$ are solvated. The latter is the case for the vast majority of molecules, as well as for van der Waals complexes and non-metallic atoms in the ground state, all of which reside in the middle of the droplet. For alkali atoms λ is

less than unity, and therefore, they are believed to form a “dimple” structure on the surface of liquid helium [22].

Mass Depletion Spectroscopy

Mass depletion spectroscopy is a technique commonly used to measure spectra of molecules embedded in helium droplets. It relies on the fact that optical excitation absorbed by the dopant is transferred to collective modes of helium bath and eventually dissipated by quantum evaporation of helium atoms from the surface of the droplet, thus. This process is schematically illustrated in Figure 2-3. The depletion of the beam can be detected either by directly observing the loss of droplet mass (as in experiments involving bolometer [7]), or by monitoring the decrease in detection probability (e.g. when using an electron impact ionizer). In both cases the depleted portion of the beam manifests itself as a characteristic dip in the observed signal, similar to the one pictured in Figure 2-4. The excitation spectrum of the dopant is recorded by scanning the laser wavelength and measuring the magnitude of this dip.

All the experiments described in this dissertation involve the use of a quadrupole mass spectrometer with electron impact ionizer. In this technique, the droplet ionization probability is a measure of the beam depletion. This probability is proportional to the geometric cross section of the droplet [23], which varies as $N^{2/3}$,

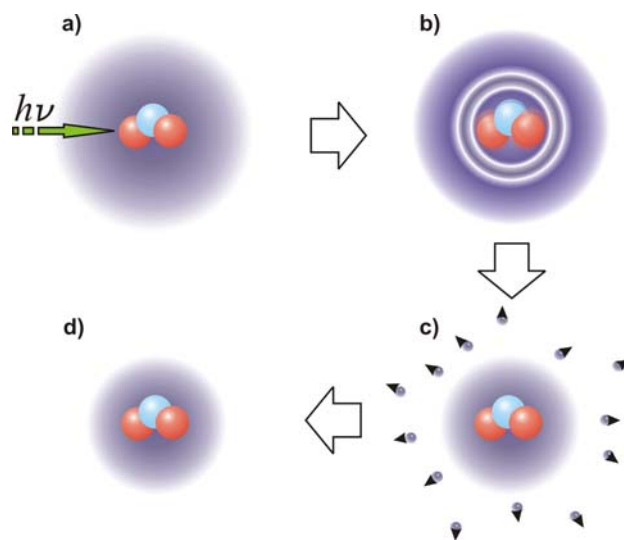


Figure 2-3. Depletion sequence for a droplet doped with NO_2 . a) – absorption of a photon; b) – relaxation into helium modes; c) – evaporative cooling; d) – “shrunk” droplet

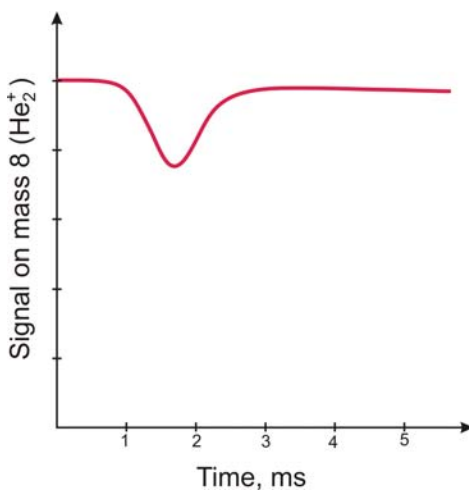


Figure 2-4. Typical depletion signal, observed at mass 8 (He_2^+) during the characteristic experimental time. Dip around 2 ms corresponds to arrival of depleted droplets at the ionization region

where N is the average number of atoms in the droplet. With each helium atom requiring about 5 cm^{-1} for evaporation, the absorption of a 575 nm photon by a $\bar{N} = 8500$ droplet would evaporate approximately 3500 atoms and result in $\frac{(8500)^{2/3} - (5000)^{2/3}}{(8500)^{2/3}} = 30\%$ depletion. However, the observed decrease in the

mass spectrometer signal at resonances of NO_2 molecule is rather modest – 10 % at most. This can be explained by the fact that not all the doped droplets absorb, in fact only about 30% do. Appendix A describes the probabilistic method of estimating the absorbing fraction from the depletion of the beam.

Helium Droplet Machine

The core elements of the experimental apparatus employed in this work were designed and built in the group of Professor C. Wittig in 2000, and have been described in detail previously [24]. The apparatus itself represents the common type of helium droplet beam machine, which is being used in several research groups around the world [5].

The overall schematic and the dimensions of the helium machine are shown in Figure 2-5. It consists of three differentially chambers: the source chamber (I), where the beam of helium droplets is produced; the pickup chamber (II), where the pickup cell is located; and the detection chamber (III), where the droplets are ionized and detected by the quadrupole mass spectrometer. Due to high volume of residual helium gas in it, the source chamber is pumped down by a 6000 l/s diffusion pump (Edwards Diffstak). This enables pressures of 10^{-6} mbar to be achieved. A 400 μm skimmer (Beam Dynamics, Model 2) separates the source chamber from the pickup chamber, which is kept at 10^{-8} mbar by means of a turbomolecular pump (Leybold Turbovac). The detection chamber is separated from the rest of the machine by a gate valve (MDC Vacuum), and is kept at 10^{-9} mbar.

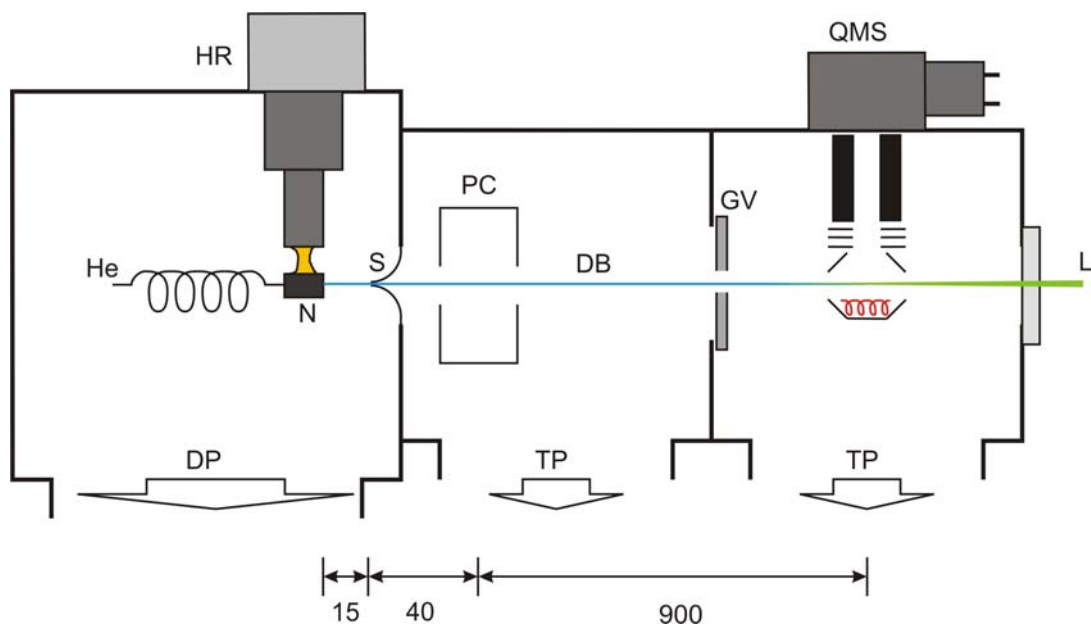


Figure 2-5. Schematic representation of the experimental setup. Dimensions in mm. He – helium supply; N – nozzle assembly; S – skimmer; HR – closed cycle helium refrigerator; PC – pickup cell; DB – droplet beam; GV – gate valve; QMS – quadrupole mass spectrometer; L – laser beam; DP – diffusion pump; TP – turbo-molecular pump

The beam of helium droplets is produced by expanding helium gas (Matheson Tri Gas, 99.9999% pure) through a $5\mu\text{m}$ aperture (National Aperture) into the vacuum. The pressure of helium before expansion can be varied from 10 to 60 atm. The gas is pre-cooled in the cryogenic nozzle assembly down to 14.5-16 K by means of a closed-cycle helium refrigerator (Advanced Research Systems), which is connected to the assembly by a braid of copper wires. Figure 2-6 schematically shows the details. A significant improvement in cooling and temperature control was brought about by the use of a copper radiation shield, attached to the first stage (30 K) of the refrigerator, and a resistive heater, attached

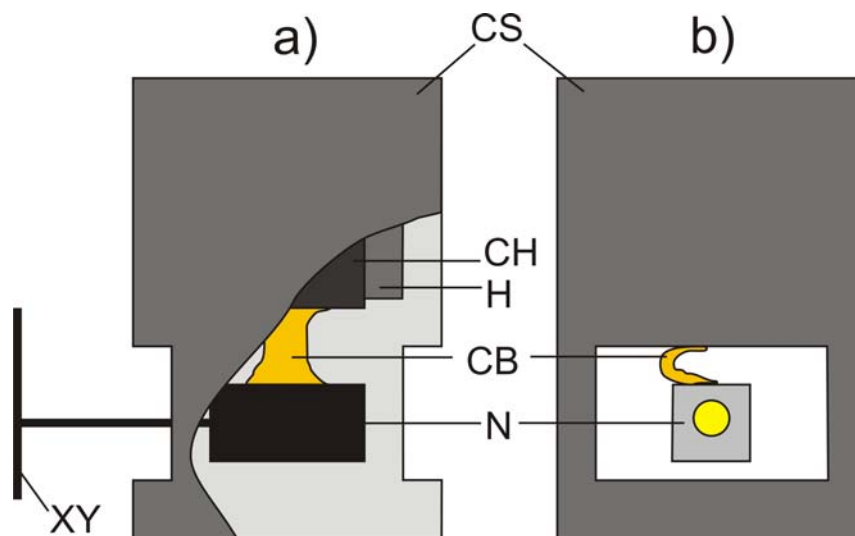


Figure 2-6. Droplet beam source assembly; a – side view, b – front view. CS – copper shield; CH – cold head; H – resistive heater; CB – copper braid; N – nozzle assembly; XY – XY positioning stage

to the second stage (4K). This arrangement allows temperature variation from 12 – 20 K. The temperature of the nozzle assembly, as well as the level of heating, are monitored and controlled by the autotuning temperature controller (Lakeshore Cryotronics, Model 321).

The doping of the helium droplets is carried out by passing the beam through a 4 cm long pickup cell, filled with molecules of the substance to be investigated. By varying the pressure in this cell is it possible to control the average number of impurity species picked up by the droplets as they pass through. This pressure is measured with a micro-ion gauge (Granville Phillips).

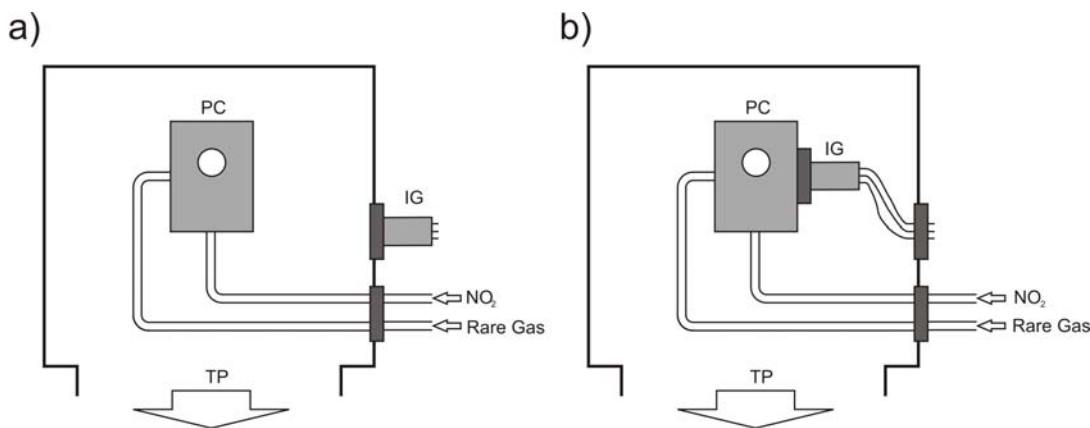


Figure 2-7. Pickup cell (PC) arrangement in chamber II (droplet beam is perpendicular to the plane of the figure): a) – ion gauge (IG) measuring overall pressure in chamber II; b) – ion gauge attached to the cell.

The pickup cell is a rectangular stainless steel box with two round openings, mounted inside of the chamber II so that droplets enter through one opening and exit through the other. The investigated gas is dosed into the cell through ¼” stainless steel tubing. A constant number-density of gas molecules is achieved through equilibrium between dosing speed, diffusion of gas from the cell into the chamber II, and pumping speed of turbo-molecular pump. Therefore, the relative position of the pressure gauge with respect to the pickup cell affects the measurement of actual number-density in the cell. Two different “pickup cell – pressure gauge” arrangements were used during the course of the studies described in this dissertation. Figure 2-7a shows the initial arrangement, in which the ion gauge is measuring the pressure change in the whole chamber II. This results in systematically lower readings than the actual pickup cell pressure (e.g. 10^{-8} mbar vs.

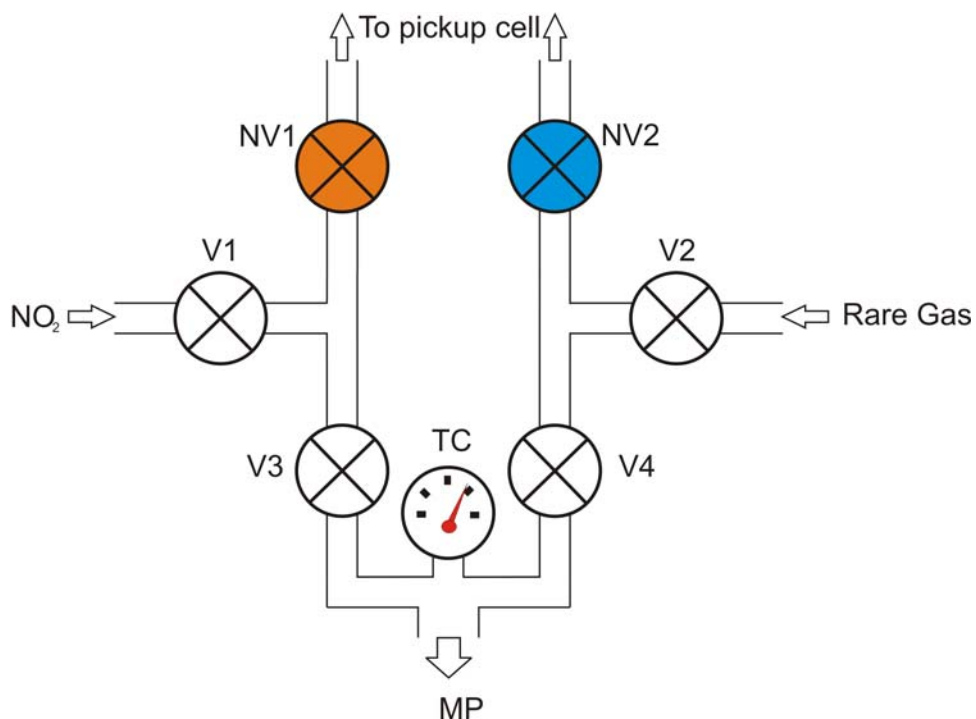


Figure 2-8. Gas dosing line. V1 – V4 – quarter-turn valves; NV1, NV2 – precision leak valves; TC – thermocouple pressure gauge; MP – mechanical pump

10^{-6} mbar). Therefore, the design was modified. As shown in Figure 2-7b, the ion gauge was directly connected to the pickup cell through a 1.33" ConFlat® flange. Gauge readings are received outside the chamber via a set of copper wires and an electrical feed-through.

The studies described in this work require the addition of two different species into the pickup cell: NO_2 (Matheson Tri Gas, 99.5% pure) and a rare gas species (Ne, Ar, Kr, Xe, all – Matheson Tri Gas, research grade). The gas line used for this purpose, is shown in Figure 2-8. By means of a system of quarter-turn

valves (Swagelok), the whole line, or any of its two halves separately, can be evacuated by a mechanical pump (Varian DS 202) down to pressures of $\sim 10^{-2}$ mbar. The line allows quick switching between three doping regimes: only NO₂, only rare gas, or both. Precise dosing of the gas is carried out by means of two needle-valves (Leybold).

The beam of droplets is analyzed in the quadrupole mass spectrometer (Balzers). The axis of the mass filter is positioned perpendicular to the droplet beam to allow for the laser beam to be directed counter-propagating to the droplet beam, thus allowing for maximum overlap of the two beams.

The laser radiation in the range 560 – 580 nm is produced by a tunable fluorescence dye laser (ND 6000, Continuum), pumped by the second harmonic (532 nm) of the pulsed Nd:YAG laser (Powerlite 9020, Continuum). The following dyes were used: Rhodamine 590, Rhodamine 610, Rhodamine 640 (all – Exciton, Inc.), as well as their mixtures. The output power is typically 60 – 80 mJ per pulse.

References and Notes

1. G. Scoles, *Atomic and Molecular Beam Methods, Vol. 1, 2*, Oxford University Press, New York (1988)
2. L. Andrews, M. Moskovits, *Chemistry and Physics of Matrix-isolated Species*, North Holland, Amsterdam, 1989, p. 430
3. F. Bolduan, H. J. Jodl, *J. Mol. Spec.*, 91, 404 (1982)
4. J. Wilks, D. S. Betts, *An Introduction to Liquid Helium*, Clarendon Press, Oxford (1987)
5. J. P. Toennies, A. F. Vilesov, *Annu. Rev. Phys. Chem.* 49, 1 (1998) and references therein
6. J. P. Toennies, A. F. Vilesov, *Angew. Chem. Int. Ed.* 43, 2622 (2004) and references therein
7. C. Callegari, K. K. Lehmann, R. Schmied, G. Scoles, *J. Chem. Phys.* 115, 22 (2001)
8. F. Stienkemeier, K. K. Lehmann, *J. of Phys. B: At. Mol. Opt. Phys.*, 39, R127-R166 (2006)
9. M. Y. Choi, G. E. Douberly, T. M. Falconer, W. K. Lewis, C. M. Lindsay, J. M. Merritt, P. L. Stiles, R. E. Miller, *Int. Rev. Phys. Chem.*, 25, 1&2 (2006)
10. H. Kamerlingh Onnes, *Commun. Phys. Lab. Univ. Leiden* 105, 744 (1908)
11. E. W. Becker, R. Klingelhöfer, P. Lohse, *Z. Naturforsch. A* 16, 1259 (1961)
12. J. Harms, J. P. Toennies, F. Dalfovo, *Phys. Rev. B* 58, 3341 (1998)
13. D. M. Brink, S. Stringari, *Z. Phys. D*, 15, 257 (1990)
14. M. Hartmann, R. E. Miller, J. P. Toennies, A. Vilesov, *Phys. Rev. Lett.* 75, 1566 - 1569 (1995)
15. K. B. Whaley, *Int. Rev. Phys. Chem.* 13, 41 (1994)

16. J. Harms, J. P. Toennies, Phys. Rev. B 63, 184513 (2001)
17. U. Henne, J. P. Toennies, J. Chem. Phys. 108, 9327-38 (1998)
18. A. Scheidemann, J. P. Toennies, J. A. Northby, Phys. Rev. Lett. 64, 1899 (1990)
19. M. Lewerenz, B. Schilling, J. P. Toennies, J. Chem. Phys. 102, 8191 (1995)
20. N. Pörtner, A. F. Vilesov, M. Havenith, Chem. Phys. Lett. 343, 281 (2001)
21. Ancilotto, F. and P.B. Lerner, J. Low Temp. Phys. 101, 1123 (1995)
22. Stienkemeier, F. and A. Vilesov, J. Chem. Phys. 115(22), 10119 (2001)
23. H. Deutsch, K. Becker, T.D. Märk. Int. J. Mass Spectrom. Ion Processes 144, L9-L12 (1987)
24. E. Polyakova, "Multiphoton ionization of molecules, embedded in superfluid helium droplets", PhD Dissertation, University of Southern California (2005)

III. Visible Spectroscopy of NO₂ in Helium

Droplets

Electronic Spectroscopy in Helium Droplets

Electronic spectroscopy of atoms and molecules embedded in He droplets is a sensitive experimental technique which provides a wealth of information about structure and dynamics of helium environment [1]. This is largely due to the fact that unlike rovibrational, electronic excitations often induce large changes in helium-impurity interaction potential. For different species, however, the situation may span a wide range. Two important and qualitatively different cases are described further in this section: the electronic excitations of metal atoms and organic molecules embedded in helium droplets. The case of NO₂ molecule is then compared and discussed in greater detail.

Interactions of liquid helium with *metal atoms* are dominated by strong Pauli repulsion with the outer shell electron. Upon excitation the electron density is pushed further out, which causes a considerable change in the equilibrium configuration of the surrounding helium. Spectroscopic studies of metals in bulk liquid helium [2, 3] revealed very broad line shapes of 50-300 cm⁻¹ FWHM, which

were significantly blue shifted ($500\text{-}1500\text{ cm}^{-1}$) relative to those of a free atom. Such robust interaction also dictates a special ground state configuration: solvated metal atoms reside in a void, similar to that occupied by an electron in liquid helium [4], albeit somewhat smaller in diameter ($10\text{-}20\text{ \AA}$ vs. 34 \AA). In droplet beam experiments, the location of the metal atom in or on the droplet can be deduced from the corresponding absorption spectra. Electronic spectra of metals such as Al [5] and Mg [6] showed very close resemblance to those recorded in bulk helium. This suggested that these species are fully immersed in the droplet. The electronic excitation, however, may change the equilibrium configuration to such an extent that it leads to ejection of the atom from the droplet, as it has been observed for Ag [7]. All of the alkali atoms have been found to reside on the surface [8] (narrower and less shifted spectra), while alkaline earth metals are believed to be inside the droplet, but close to the surface [9].

The change in the helium-impurity interaction is more intricate in case of electronic excitations of *organic molecules* in helium droplets [1]. Factors specific to each molecule, such as polarizability, location of the molecule's chromophore, structure of the closest helium shell, etc, strongly affect this interaction. This leads to qualitatively different line shifts, which vary from moderately blue, as in the case of benzene [10], to moderately red, as for phthalocyanine and tetracene [1, 11]. The overall perturbation is generally modest and is due to the intravalent character of the lowest electronic excitations (*i.e.*, $S_1 \leftarrow S_0$) in organic molecules. These transitions

result in changes in the nodal structure of the electronic wave function, rather than increase the electronic density in the outer region. The coupling to the surrounding medium is weak and the spectrum consists of narrow zero phonon lines accompanied by low-intensity phonon wings. This property makes molecules such as glyoxal a unique microscopic probe for the elementary excitations of liquid helium which constitute the phonon wing [12].

The nature of electronically excited states of *nitrogen dioxide* molecule differs substantially from both of the above examples. The conical intersection of the zero-order X^2A_1 ground electronic state with zero-order A^2B_2 excited electronic state results in strong non-adiabatic coupling and the intramolecular vibronic chaos. Gas-phase spectrum of NO_2 is well-studied in the whole spectral range, making the molecule a good benchmarking system [13]. It has been shown that in helium droplets the overall character of the gas-phase spectrum is preserved [14], although each and every line is blue-shifted by 7 cm^{-1} and broadened by 7 cm^{-1} (Figure 3-1). This suggests that the intramolecular dynamics is robust and is not compromised by interaction with the helium host. Yet the helium-induced relaxation is fast enough to suggest efficient coupling.

In the following sections, the mechanisms that can account for observed shifts and widths of the spectral lines of nitrogen dioxide in helium droplets are discussed. The developed models can then be applied to explain the main

experimental results of this work – mass-depletion spectroscopy of droplets doped with NO₂ and rare gas atoms (Ne, Ar, Kr and Xe).

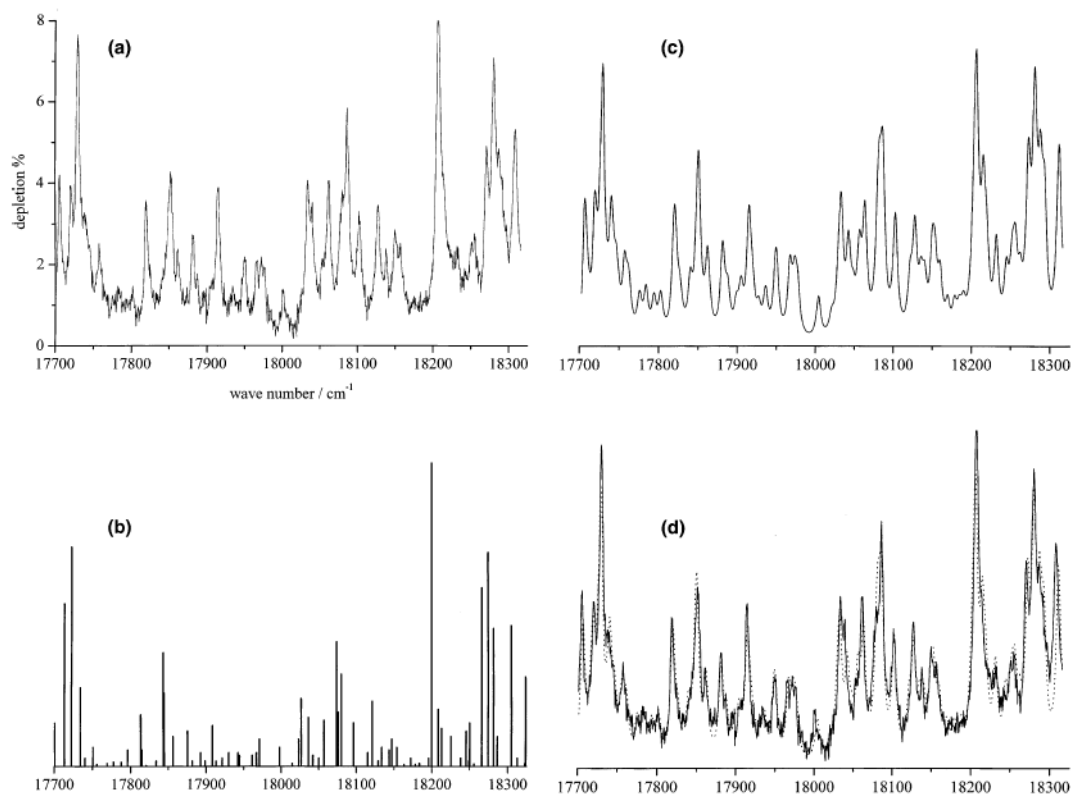


Figure 3-1. (a) Mass-depletion spectrum of NO₂ in helium droplets ($\sim 10^4$ atoms per droplet), from ref. [14]. (b) LIF spectrum of NO₂ in the same energy region, from [15]. (c) All of the lines in (b) have been assigned 7 cm⁻¹ widths and blue-shifted by 7 cm⁻¹. The intensities are fitted to the experimental spectrum. (d) The experimental and simulated spectra are overlapped.

Shifts

In order to build a qualitative understanding of the origins of the 7 cm⁻¹ line shift, it is informative to consider the character of the excited states of NO₂. In the range 16500 – 18300 cm⁻¹ each of these states is a combination of zero-order X²A₁ and A²B₂ electronic states. The expansion of an NO₂ eigenstate ψ_i in a basis built from X²A₁ and A²B₂ electronic states and vibrations therein is given by:

$$\psi_i = \sum_k C_{ik}^A \psi^A \chi_k^A + \sum_l C_{il}^X \psi^X \chi_l^X \quad (1)$$

where ψ^X and ψ^A are the electronic wave functions for the X²A₁ and A²B₂ states, respectively, and χ_l^X χ_k^A are the vibrational wave functions within respective electronic spaces. Because of the chaotic nature of the intramolecular vibronic dynamics, the coefficients C_{il}^X and C_{ik}^A can be taken as random real numbers subject to normalization. A statistical assumption can be used to obtain the average participation of the zero-order states in the molecular eigenstates. Namely, the average percentage of X²A₁ character can be estimated as $\frac{\rho_X}{\rho_X + \rho_A}$, where ρ_X and

ρ_A are the densities of X²A₁ and A²B₂ states, respectively, in the energy range of 16500 – 18300 cm⁻¹. These energies lie significantly higher than the origin of the A²B₂ state (around 9000 cm⁻¹) or the bottom of the conical intersection (around 1000 cm⁻¹), which means that all degrees of freedom, electronic as well as

vibrational, are *thoroughly mixed by non-adiabatic coupling* [15]. This mixing, in turn, justifies the statistical assumption made above, although the density of vibrational states of A^2B_2 is too small to be well-defined in this region.

According to the Georges *et al* [15], the respective densities of vibrational states of X^2A_1 and A^2B_2 are approximately 0.20 and 0.03 per cm^{-1} in the interval of 16500 – 18500 cm^{-1} . This makes the resulting eigenstates bear ~87% of the X^2A_1 character and ~13% of the A^2B_2 . This estimate, combined with the valence character of A^2B_2 leads to the conclusion that it is not the extension of electron density upon excitation that causes the blue shift. The eigenstates are better visualized in terms of high-quanta vibrational states of X^2A_1 . For the analysis presented here the most important characteristic of such states is their *increased effective size*. Even diagonal anharmonicity can cause the mean displacements of the vibrational coordinates to increase with energy. But more importantly, the outer turning points of the excited vibrational levels spread with energy, and this spread is larger than (and subsumes) that is due to anharmonicity, as illustrated in the Figure 3-2.

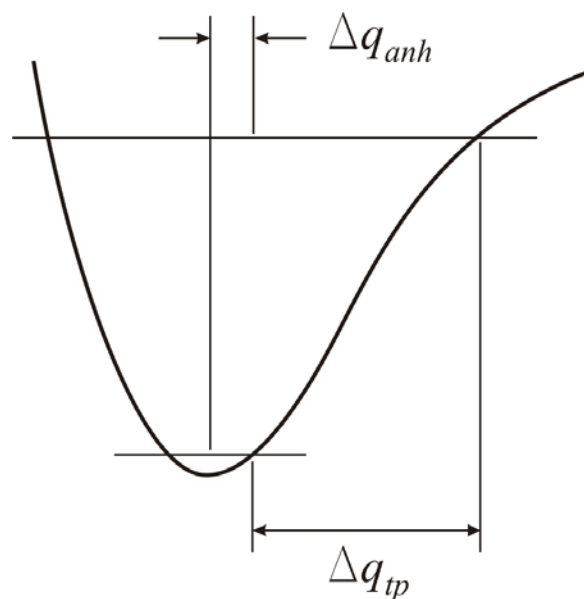


Figure 3-2. Diagonal anharmonicity results in an increase in the average displacement of a vibrational state: Δq_{anh} . The outer turning point increases with vibrational excitation: Δq_{tp} . When the vibration is rapid relative to the response time of the surrounding medium, the outer turning point determines the effective size of the embedded moiety.

To qualitatively describe the interaction of such enlarged state with helium bath it is useful to introduce a separation of coupling strengths and associated timescales. Processes that are intra-molecular to NO_2 are the fastest and most robust. Interaction of NO_2 with its surrounding non-superfluid shell comes next. Last is the coupling of NO_2 and its helium shell to the surrounding superfluid. The relatively rapid NO_2 vibrations increase the size of molecules periphery, and helium with its weak binding to NO_2 cannot follow the molecule's nuclear degrees of freedom. The helium maintains its distance from the outer turning points. This qualitative separation is shown schematically in the Figure 3-3.

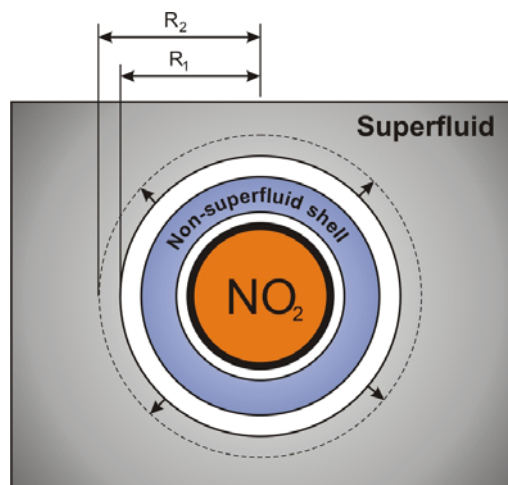


Figure 3-3. NO₂-Helium dynamics: separation of couplings and corresponding timescales. Excitation pushes surrounding superfluid from R₁ to R₂.

From the perspective of the NO₂ chromophore the increase of its size causes it to push against the surrounding helium. It is known that photoexcitation to a repulsive part of the potential curve can result in blue-shift and broadening, according to what is called a *reflection principle*. The general idea is schematically illustrated in Figure 3-4 (a) in terms of a possible NO₂-Helium potential. However, such excitations would involve larger blue-shifts (*i.e.*, hundreds of cm⁻¹), as in the case of metal atoms described above. It is improbable that 7 cm⁻¹ blue shift observed in the case of NO₂ is due to reflection principle shown in Fig. 3-4 (a). More importantly, the transitions of the type depicted in Figure 3-4 (a) induce large collective excitations of the helium environment and, hence, are accompanied by large inhomogeneous broadening. The observed line shapes of NO₂, in contrast, can be well fitted with smooth lorentzians of 7 cm⁻¹ width.

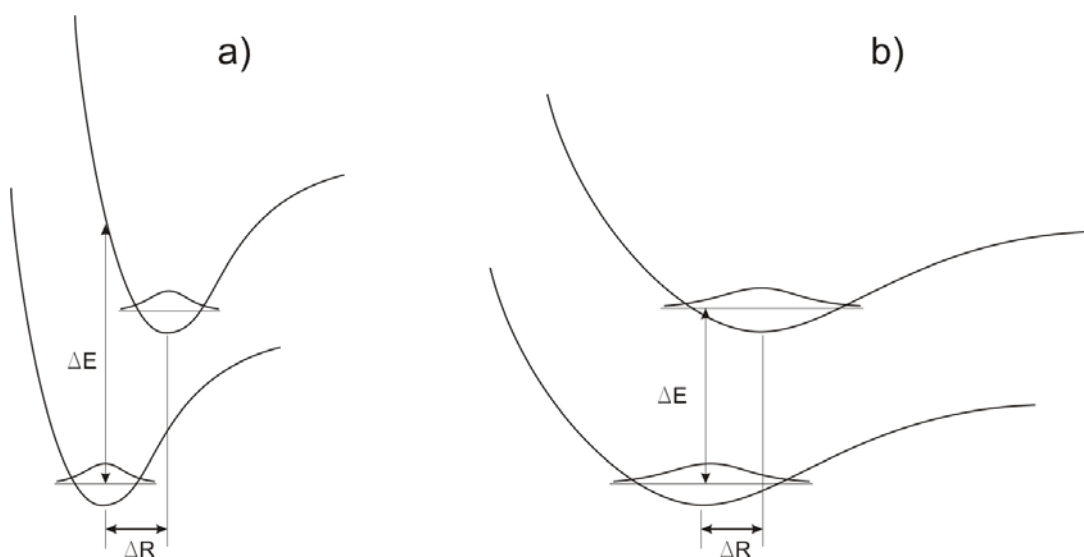


Figure 3-4. NO₂-Helium potential in ground and excited states. Scenario in b) with shallow potential and good overlap between ground and excited state wave functions describes the observed shifts and widths better than that in a), which implies broad Franck-Condon envelope.

On the basis of the above considerations it can be concluded that the mechanism shown in Figure 3-4 (a) cannot be responsible for the blue shift observed in the photoexcitation of NO₂ in helium droplets. By no means can the wave function for the NO₂-Helium coordinates be as localized as it is demanded by this picture. Figure 3-4 (b) is a better candidate as it reflects the core characteristics of the NO₂-Helium potential that can be inferred from the experiment:

- the potential is shallow and the wave function spread over a large distance

- the overlap between the ground and excited state NO₂-helium wave functions is sufficiently large, so that transition occurs with only modest helium excitations.

The blue shift can now be looked at as simply the extra energy needed to increase the size of the cavity occupied by NO₂ and its closest helium shell in the surrounding superfluid. A simple calculation of the cavity surface energy gain when going from R₁ to R₂ (referring to Figure 3-3) can provide a good supporting argument. Neglecting the pressure-volume work due to the very small pressure inside the droplet, the energy gain can be estimated as:

$$\Delta E = 4\pi(R_2^2 - R_1^2)\sigma, \quad (2)$$

where $\sigma = 3.7 \cdot 10^{-4}$ N/m is the experimental value of the surface tension at 0.37 K [16]. The size of the cavity can be assessed from the calculated properties of similar solvated molecules [17, 18]. Putting R₁ = 3 Å and R₂ = 3.3 Å, the energy to enlarge the cavity in liquid helium is approximately $\Delta E = 5.5 \text{ cm}^{-1}$, which is the order of magnitude of the observed shift.

Theoretical model

Effective Hamiltonian is sought that operates within the space of NO₂ states and treats everything else as lying outside this space. This invites a separation of the Hilbert space into two subspaces. The total Hamiltonian H is expressed as $H_0 + V$, where H_0 describes unperturbed NO₂ and V is due to the helium host. As discussed below, V is complicated.

Figure 3-5(a) shows an unperturbed NO₂ state ψ_i and Fig. 3-5(b) shows its lower-energy nearest neighbor ψ_{i-1} together with the accompanying helium excitations of ψ_{i-1} indicated by the shaded region. It is assumed that the helium that accompanies ψ_i is unexcited. There are, of course, helium excitations associated with ψ_i , but ground state helium is assigned to accompany ψ_i in accord with the model shown in Fig. 3-4(b). Thus, the collection of NO₂ levels that constitute the privileged subspace is made up of levels like ψ_i , i.e., ones that have ground state helium excitations. The space of helium excitations that lie outside the privileged subspace is like Fig. 3-5(b). Of course ψ_i can also couple to progressively lower energy NO₂ states: ψ_{i-2} , ψ_{i-3} , etc., each having its own accompanying helium excitations.

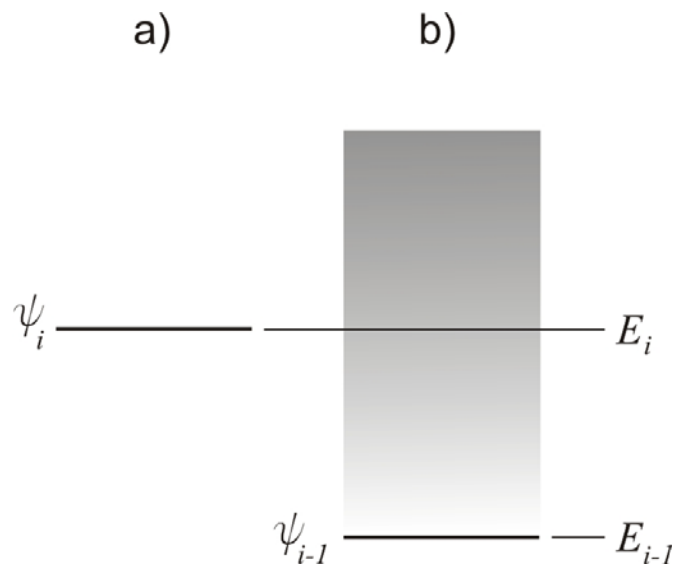


Figure 3-5. ψ_i eigenstate is coupled to the lower-energy nearest neighbor ψ_{i-1} and helium excitations associated with it.

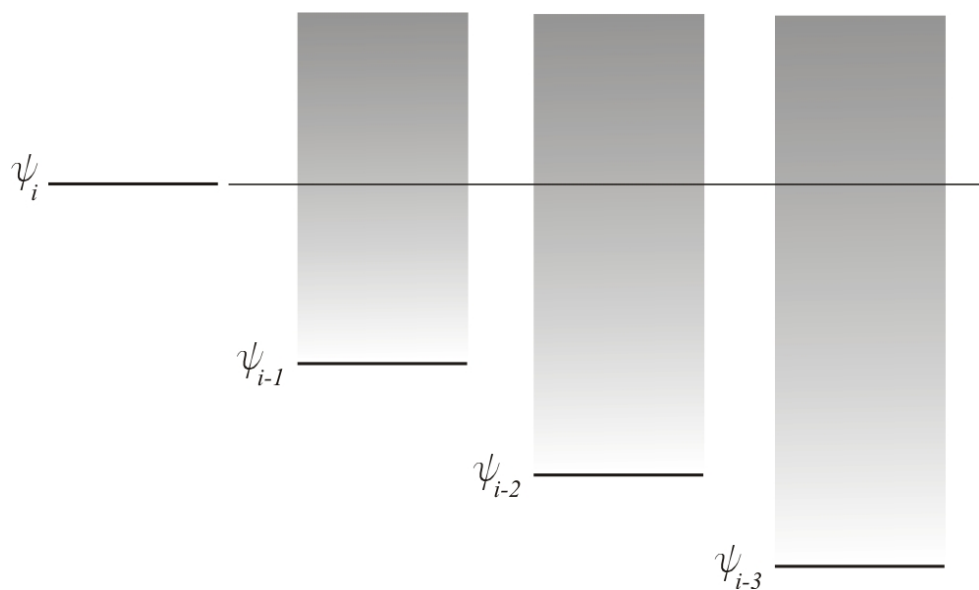


Figure 3-6. Total decay width of ψ_i is the sum of the partial widths for all of the open decay channels.

Determination of the helium density of states is confounded at low energies by the fact that the helium shell that encrusts NO₂ is not superfluid. It can have low-energy vibrations that are more-or-less local to the helium that is immediately adjacent to the NO₂. The superfluid lies beyond this shell, and presumably there is transition region between the encrusted and superfluid limits. At energies of several tens of cm⁻¹ or more, the helium density of states will be continuous. In consideration of the above points, the shaded region in Fig. 3-5 should be construed as highly schematic.

The effective Hamiltonian for the NO₂ space is given by [19]:

$$H^{eff} = Q \left(H_0 + V + VP \frac{1}{E - H_0 - V} PV \right) Q \quad (3)$$

where Q and P are orthogonal projectors onto the NO₂ and helium spaces, respectively. This expression is exact but not user-friendly because of the E in the denominator. H^{eff} operates solely within the space of NO₂ states (the Q -space), and all interactions between the helium host and NO₂ are accounted for with V . As mentioned above, a considerable amount of physics is contained in V . It has matrix elements within the Q -space as well as between the Q and P -spaces. It includes the helium that immediately surrounds the NO₂, the more distant superfluid, and anything in between. We shall make no attempt to determine V as this lies beyond our abilities. The conclusions that will be drawn are based on general considerations.

The diagonal matrix elements of H^{eff} , correct to second order in V , are given by:

$$H_{ii}^{eff} = E_i + V_{ii} + \sum_n \int dE \cdot \rho_{He}(E) \frac{|V_{in}|^2}{E_i - E_n - E} \quad (4)$$

In this expression, the lower NO₂ states (one of which is indicated in Fig. 3-5(a)) are labeled n , and the energy E is measured relative to E_n . The sum over n includes all diagrams such as Fig. 3-5(b). For each lower NO₂ state there exist helium excitations that are accounted for by the integration. This scenario in which ψ_i is coupled to lower NO₂ states and their helium excitations is shown in Fig. 3-6. The matrix element V_{in} includes both NO₂ and helium.

Referring to Eq. (4), the first two terms on the right hand side are straightforward. They are the energy of the unperturbed ψ_i level and the first order correction to the energy brought about by V acting within the Q-space. The remaining term requires care because the range of integration includes the point where the denominator is zero. Equation (4) is simplified, however, when the helium excitations are taken as continuous with a smooth density of states, in which case the diagonal matrix elements become:

$$H_{ii}^{eff} = E_i + V_{ii} + \sum_n \left\{ P \int_{-\infty}^{+\infty} dE \cdot \rho_{He}^n(E) \frac{|V_{in}|^2}{E_i - E_n - E} - \frac{i}{2} \sum_n 2\pi \cdot \rho_{He}^n(E) \cdot |V_{in}|^2 \right\} \quad (5)$$

P here denotes principal part integration. This term does not play a significant role because $\rho_{He}^n(E) \cdot |V_{in}|^2$ does not vary rapidly near E_i . Thus, it shall be set equal to zero. This leaves V_{ii} , which is the change of the energy of ψ_i brought about by the helium, and the imaginary term that is $-i/2$ times the linewidth, $\hbar\Gamma_i$:

$$\hbar\Gamma_i = \sum_n 2\pi \cdot \rho_{He}^n(E) \cdot |V_{in}|^2 = \sum_n \hbar\Gamma_{in} \quad (6)$$

The total decay width of ψ_i is the sum of the partial widths for the lower NO₂ levels ψ_n , i.e., the partial widths for all of the open decay channels.

The term V_{ii} is now discussed in terms of observed line shifts. The fact that all line shifts observed in the above mentioned energy range are within the 2 cm⁻¹ of the central value of 7 cm⁻¹ can be explained in terms of the chaotic nature of NO₂ vibrations. The interactions between the NO₂ eigenstates can be given as matrix elements:

$$V_{ij} = \langle \psi_i | V | \psi_j \rangle. \quad (7)$$

We shall make no attempt to determine V as this lies beyond our abilities. The conclusions that will be drawn are based on general consideration. Using the expression for NO₂ wave functions in (1), Eqn. (7) becomes:

$$V_{ij} = \left\langle \sum_k C_{ik}^A \psi^A \chi_k^A + \sum_l C_{il}^X \psi^X \chi_l^X \middle| V \middle| \sum_{k'} C_{jk'}^A \psi^A \chi_{k'}^A + \sum_{l'} C_{jl'}^X \psi^X \chi_{l'}^X \right\rangle \quad (8)$$

Equation (8) can be simplified by using the fact that NO₂ states are quantum chaotic. Consider only the term for the A²B₂ state:

$$\left\langle \sum_k C_{ik}^A \psi^A \chi_k^A \middle| V \middle| \sum_{k'} C_{jk'}^A \psi^A \chi_{k'}^A \right\rangle \quad (9)$$

It is assumed that V is not responsible for additional non-adiabatic coupling other than that is brought about by conical intersection. Were it not the case, it would not have been possible to fit the line positions with a single value of the shift. Thus, $V\psi^A = \psi^A V$ and the integration over electron coordinates gives unity.

Equation (9) therefore reduces to

$$\sum_{k,k'} C_{ik}^A C_{jk'}^A \langle \chi_k^A | V | \chi_{k'}^A \rangle \quad (10)$$

Chaotic nature of the intramolecular dynamics dictates the random choice of the expansion coefficients. This leads to a high degree of cancellation that occurs when carrying out summations for $i \neq j$. Off-diagonal matrix elements are therefore assumed negligible, and the dominant surviving term has $i = j$ and $k' = k$:

$$\sum_k |C_{ik}^A|^2 V_{kk} \quad (11)$$

It is seen that the diagonal terms ($i = j$) are weighted sums of expectation values for different vibrational states within the A²B₂ electronic state. The same argument applies to the integrations in Eqn. (8) associated with the X²A₁ state. In this case, the dominant surviving term is:

$$\sum_l |C_{il}^X|^2 V_{ll} \quad (12)$$

Referring to Eqn. (8), the terms between the X^2A_1 and A^2B_2 states vanish because, as stated above, V is not responsible for non-adiabatic coupling beyond that induced by conical intersection. Thus, the net energy shift is given by:

$$\Delta E \approx \sum_k |C_{ik}^A|^2 V_{kk} + \sum_l |C_{il}^X|^2 V_{ll} \quad (13)$$

The V_{kk} and V_{ll} are independent of the compositions of the individual eigenstates, which are embodied in the expansion coefficients. Chaotic dynamics causes the interaction of each eigenstates with helium environment to be averaged over the vibrational phase space. The amount of shift is the same for each eigenstate due to this averaging.

References and Notes

1. F. Stienkemeier, A. Vilesov, *J. Chem. Phys.* 115, 10119 (2001)
2. B. Tabbert, H. Gunther, G. zu Putlitz, *J. Low Temp. Phys.* 109, 653 (1997)
3. H. Bauer, M. Beau, B. Friedl, C. Marchand, K. Miltner, H.J. Reyher, *Physics Letters A* 146 (3), 134 (1995)
4. K. Hiroike, N.R. Kestner, S.A. Rice, J. Jortner, *J. Chem. Phys.* 43(8), 2625 (1965)
5. J. Reho, U. Merker, M.R. Radcliff, K. Lehmann, G. Scoles, *J. Phys. Chem. A* 104, 3620 (2000)
6. J. Reho, U. Merker, M.R. Radcliff, K. Lehmann, G. Scoles, *J. Phys. Chem.* 112, 8409 (2000)
7. F. Federmann, K. Hoffmann, N. Quaas, J.D. Close, *Phys. Rev. Lett* 83, 2548 (1999)
8. F. Stienkemeier, J. Higgins, C. Callegari, S.I. Kanorsky, W.E. Ernst, G. Scoles, *Z. Phys. D* 38, 253 (1996)
9. F. Stienkemeier, F. Meier, H.O. Lutz, *J. Chem. Phys.* 107(24), 10816 (1997)
10. R. Schmied, P. Carcabal, A.M. Dokter, V.P.A. Lonij, K.K. Lehmann, G. Scoles, *J. Chem. Phys.* 121(6), 2701 (2004)
11. M. Hartmann, A. Lindinger, J.P. Toennies, A.F. Vilesov, *Chem. Phys.* 239, 139 (1998)
12. M. Hartmann, F. Mielke, J. P. Toennies, A. Vilesov, G. Benedek, *Phys. Rev. Lett.* 76, 4560 (1996)
13. A. Delon, R. Jost, M. Jacon, *J. Chem. Phys.* 114(1), 331 (2001)
14. E. Polyakova, D. Stolyarov, X. Zhang, V. V. Kresin, C. Wittig, *Chem. Phys. Lett.* 375(3-4), 253 (2003)
15. R. Georges, A. Delon, R. Jost, *J. Chem. Phys.* 103(5), 1732 (1995)

16. J.R. Eckardt, D.O. Edwards, S.Y. Shen, F.M. Gasparini, Phys. Rev. B 16(5), 1944 (1977)
17. F. Paesani, K.B. Whaley, J. Chem. Phys. 121(9), 4180 (2004)
18. F. Paesani, K.B. Whaley, J. Chem. Phys. 121(11), 5293 (2004)
19. C. Wittig, I. Bezel, J. Phys. Chem. B 110(40), 19850 (2006)

IV. Adding Rare Gas Atoms to Helium

Droplets Doped with NO₂

Capture and ionization of rare gas atoms within helium droplets

One of the most intriguing aspects of the helium droplet isolation technique is the pickup process. In many experiments, including the one described in this dissertation, a quadrupole mass spectrometer equipped with electron beam ionizer is used to analyze the contents of the droplet beam. Thus, our assumptions about what happens to the beam as it passes through the pick-up cell are based on our interpretation of the mass spectral data from electron impact ionization. The analysis of mass spectra is often complicated because of two major reasons. *First*, the ionization process is not as straightforward as it would be reasonable to assume, given the huge difference in ionization potentials for He and other species. Experimental studies have shown [1] that in case of large clusters (e.g. ~15000 atoms) doped with NO molecule, the probability that the product ion will contain NO⁺ is about 1/50. Rare gas atoms, having relatively large ionization energies, represent a special case of extremely low charge transfer probabilities. *Second*, the

localization of charge on an impurity atom or sub-cluster is highly exothermic. It results in extensive fragmentation to form a broad distribution of ion products, which is characteristic to a specific impurity.

A good understanding of the following subjects is needed to infer the contents of the molecular beam from the observed in the mass spectrum:

- Ionization and fragmentation of pure helium droplets
- Ionization of doped helium droplets and charge transfer to the dopant
- Fragmentation of doped droplets

Because the goal of this work is to be able to control the average number of rare gas atoms in helium droplets containing one NO₂ molecule, these subjects are discussed below.

Ionization and fragmentation of pure droplets

The ionization of a pure helium cluster can be understood as a four-step process [2]. *First*, the incident electron ionizes a helium atom somewhere inside the droplet to produce He⁺. Direct production of He_n⁺, or indirect ionization via excited states of helium, are ruled out by measurements of appearance potentials of various pure cluster fragment ions. Figure 4-1 shows that the shape of these potentials is similar to that of free helium atoms. In particular, there is a relatively small probability of producing ions with incident electron energies below 24.6 eV. *Second*, He⁺ migrates through the cluster via resonant charge transfer [3], directed

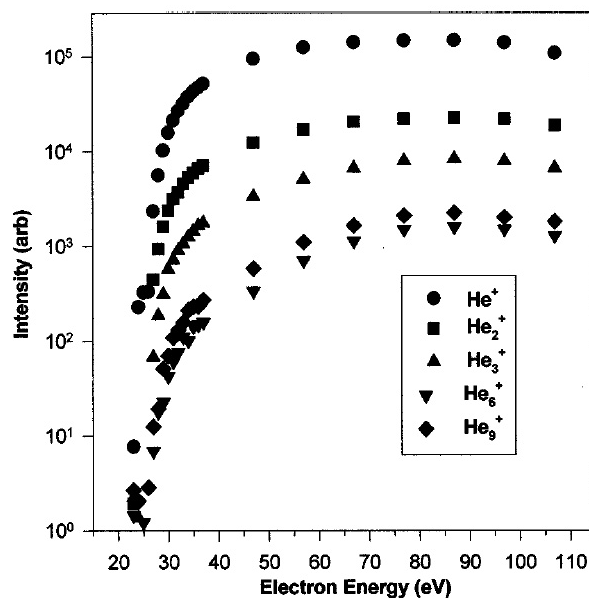


Figure 4-1. Appearance potentials of various pure cluster fragment ions compared to that of He^+ (from ref. 2)

by dielectric forces toward the center, where the electrostatic potential is lowest. The He^+ makes several “hops” before the *third step* – formation of He_2^+ , which terminates charge migration and releases 2.35 eV into the helium bath. *Finally*, extensive fragmentation breaks the cluster apart and results in the multitude of fragment ion products that are observed in the mass spectrum. Experiments by Callicoatt and co-workers [2] showed that an evaporative mechanism – a reasonable suggestion for dissipation of 2.35 eV – cannot account for the observed distribution of fragment ions. Their major result is that the probability of observing He_2^+ is nearly independent of initial cluster sizes between 1000 and 15000 atoms. Were evaporation to occur, 2.35 eV would release about 4000 atoms (0.6 meV per atom)

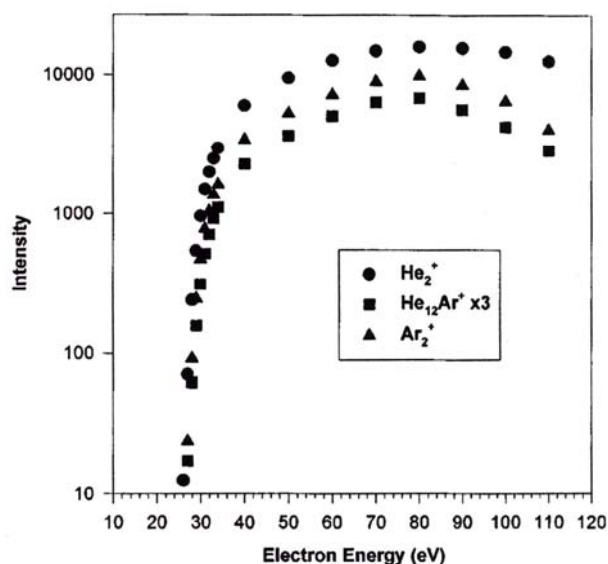


Figure 4-2. Appearance potentials for He_2^+ , He_9Ar^+ and Ar_2^+ (from ref. 5)

and the probability to observe He_2^+ would gradually decrease as the initial droplet size increased. Rather, it is suggested that the ion core is ejected from the droplet, carrying some helium atoms with it [11].

Ionization of doped helium droplets and charge transfer to the dopant

It is important to note that the probability of direct ionization of impurity atoms or molecule inside the helium droplets is small. Appearance potentials for He_2^+ , He_9Ar^+ and Ar_2^+ , presented in Figure 4-2, go asymptotically to the gas phase threshold for He^+ and are similar to the form of the He^+ excitation curve. Thus, the ionization of doped helium droplets occurs via the same four steps as described

above. The only differences are that a) the positive hole is attracted to the impurity, and b) there is finite probability of charge transfer to this impurity.

The key experimental finding, supported by theoretical modeling [1, 2, 5-8], is that the probability of charge transfer from He^+ to the impurity is less than unity and decreases dramatically with droplet size. This means that if our relatively large droplet of about 8000 helium atoms initially picked up a single impurity atom or molecule, it is unlikely that we will see this atom or molecule in the mass spectrum after this droplet is ionized by electron impact. Table 4-1 gives the charge transfer probabilities to single atoms of Ne, Ar, and Xe, as well as to NO molecule [1, 8]. The overall mechanism is the same for all these species and is responsible for similarly low probabilities in case of large droplets. The migrating positive hole travels a characteristic distance prior to self trapping, and if the path passes within a nearest neighbor of the impurity, the charge may be transferred. The bigger the droplet, the further away from impurity will be the average position of initially formed He^+ . Monte Carlo calculations for the case of Ar atom inside the droplet [4, 5] produced the best fits to the experimental results when the probability for the charge to localize on He_2^+ was set to 0.3 per “hop” of the migrating hole. This means a 50% chance of forming He_2^+ after three “hops”. Characteristic time for each “hop” was calculated at 20 fs, so that the whole charge migration occurs in 40-60 fs from the electron impact.

Table 4-1. Charge transfer probabilities from He⁺ to single impurity captured in helium droplets [1, 8].

Captured species	$\langle N \rangle = 1100$	$\langle N \rangle = 2200$	$\langle N \rangle = 3300$
Neon	0.43(1)	0.35(10)	0.06(1)
Argon	0.21(5)	0.14(3)	0.10(3)
Xenon	0.34(1)	0.34(1)	0.09(1)
	$\langle N \rangle = 540$	$\langle N \rangle = 1840$	$\langle N \rangle = 5300$
NO	0.8(1)	0.38(7)	0.15(5)

The differences in charge transfer probabilities (Table 4-1) are due to specific energetics of impurity-helium interactions. First of all, atomic polarizabilities vary by an order of magnitude through the rare gas row from Ne (2.7 au) to Xe (27.8 au) [9]. This significantly affects the chance that the migrating hole will make its next “hop” toward the impurity atom. Second, the energy released upon charge transfer varies with different ionization energies: 3.0 eV for Ne, 8.8 eV for Ar and 12.5 eV for Xe [13]. Finally, Ruchti and co-workers [8] speculate that excited electronic states of the specific impurity play an important role in the charge transfer process.

Fragmentation of doped droplets

Complex fragmentation patterns of droplets containing the atoms of rare gases can be inferred by analyzing the dependence of mass spectra on the pressure

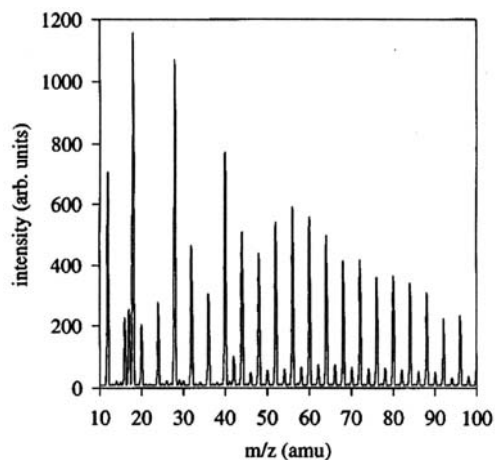


Figure 4-3. Typical mass spectrum of droplets that picked up one neon atom on average (from ref. 10)

of gas in the pickup cell [5, 6, 8, 10]. A typical mass spectrum is shown in Figure 4-3, which shows peaks corresponding to fragmentation products of droplets that picked up one neon atom on average.

One of the most interesting experimental observations is that ionization of droplets which initially had *one* neon or argon atom would never result in appearance of bare ion peak in the mass spectrum, Ne^+ or Ar^+ respectively. Instead, these droplets manifest themselves as a broad distribution of peaks He_nNe^+ or He_nAr^+ . In contrast to this, droplets that picked up *two* atoms of Ne or Ar, fragment upon ionization to yield predominantly Ne_2^+ or Ar_2^+ bare ion. Figure 4-4 shows the pickup cell pressure dependence of He_9Ar^+ (mass 76) and Ar_2^+ (mass 80) signals. The He_9Ar^+ curve is fit with the expected pressure dependence for clusters

containing only one Ar atom. Ar_2^+ curve peaks at pressure twice as high, indicating droplets carrying two atoms.

Formation of products like He_nNe^+ or He_nAr^+ is attributed to the same mechanisms as with He_n^+ . The nascent rare gas ion forms a stable complex with He, the excess energy goes to extensive fragmentation and ejection of the final ion product [11]. Although in case of Ar much more energy is available, the fragmentation pattern is very similar to the one in case of Ne. This is explained by dissipation of most of this energy by emission of a VUV photon [5]. In droplets containing two impurity atoms, charge transfer to the Ne_2 or Ar_2 leaves the ion with about 1 eV of vibrational excitation due to poor Franck-Condon overlap between neutral and ionic ground states [12]. The final fragmentation product is thus able to “shake off” excess helium atoms, producing mostly bare Ne_2^+ or Ar_2^+ . A still significant amount of He_nNe_2^+ (compared to negligible amount of respective He_nAr_2^+) products suggests that helium is more efficient in quenching neon dimer excitations.

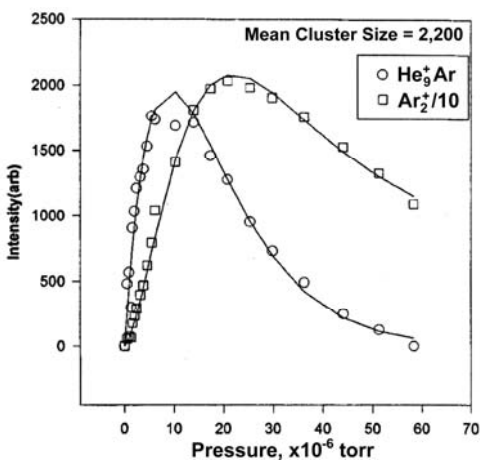


Figure 4-4 Pickup cell pressure dependence of He_9Ar^+ (mass 76) and Ar_2^+ (mass 80) signals (from ref. 5)

Droplets containing 3 or more atoms of Ar or Ne mostly fragment to form dimer ions. In case of Ar, large droplets (>8000 atoms) are able to partially suppress such fragmentation, so that some of the parent ions survive [5, 10].

In an interesting contrast to the cases of Ne and Ar is the case of droplets doped with Xe atoms [8]. Excited electronic states of Xe^+ are considered to play an important role in charge transfer process. In particular, the $^2\text{S}_{1/2}$ state of Xe^+ interacts repulsively with He. This is considered to be the major reason for the fact that the most likely product of ionization of droplets that contain one Xe atom is Xe^+ . Another difference from the cases of Ne and Ar is that although Xe_2^+ is still the most likely outcome of ionization of droplets containing dimer Xe_2 , Xe^+ is also produced with considerable probability. Again, these peculiarities are attributed to participation of excited electronic states of Xe^+ .

Calibration of the pickup cell pressure variation technique

As described in the previous section, each group of helium droplets, carrying a specific number of impurities, leaves a characteristic “fingerprint” in the mass spectrum. This allows us to monitor and control the average number of rare gas atoms picked up by the droplets by varying the pressure in the pickup cell. The goal of this section is to establish a usable relationship “pressure \leftrightarrow number of embedded atoms” for the particular experimental setup discussed in this dissertation.

Neon

By plotting the “signal vs. pressure” dependences for various ionization fragments, Callicoatt and co-workers [10] were able to define the NeHe_n^+ signals, with $3 \leq n < 5$, as coming mostly from the droplets carrying one neon atom. Ne_2^+ signal was determined as an indicator of droplets that picked up two neon atoms. Figure 4-5a shows pickup cell pressure dependence of signals at masses 36 (NeHe_4^+ , He_9^+) and 40 (Ne_2^+ , NeHe_5^+ , He_{10}^+).

To calibrate these results, the pickup process was simulated by Poisson distribution of probability I_k to pick up k number of atoms:

$$I_k(z) = \text{const} \cdot \frac{(z)^k}{k!} \exp(-z), \quad (1)$$

$$z = \sigma L \frac{P}{k_B T},$$

where z is the average number of collisions, σ is the pickup cross section of the droplet, L is the length of the pickup cell, P is the pressure of foreign species in the pickup cell, k_B is the Boltzmann constant, T is the absolute temperature of the species in the pickup cell. The following parameters of the experimental apparatus were employed (see Ch. II for detailed description): $\sigma = 6.36 \cdot 10^{-17} \text{ m}^2$, which corresponds to average droplet size of about 8500 atoms [14]; $L = 35 \text{ mm}$; $T = 295 \text{ K}$.

The resulting distributions, presented in Figure 4-5b, predict peak probabilities for pickup of neon atoms at much higher pressures than observed in the experiment. A plausible explanation for this discrepancy is based on the fact that the ionization gauge (Bayard-Alpert type), located in the pickup cell, is calibrated for nitrogen gas, N_2 . The sensitivity of this gauge for neon is smaller by a factor of ~ 4 , which had been observed in several calibration experiments [15]. Ion gauge sensitivities for several gases relative to argon are listed in the Table 4-2. This means that our gauge “lags” behind, showing small pressure while the pickup cell is in fact full of neon gas. To compensate for this “lag”, the pressure scale of the simulated curves has been divided by 4 [17].

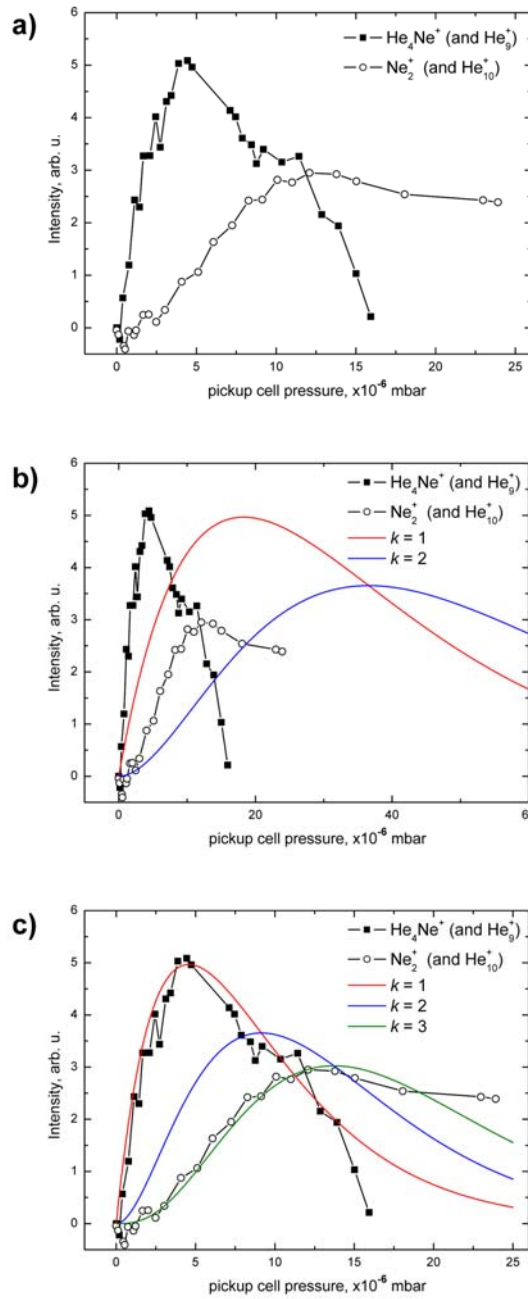


Figure 4-5. Calibration of neon pressure variation technique: a) pressure dependence of mass spectrometer signal at masses 36 and 40; b) same as a) plus simulated probability distributions (note the horizontal scale); c) same as b), with simulated distributions corrected to account for ion gauge sensitivity

Table 4-2. Ionization gauge sensitivity ratios r for various gases,
 $r = \{\text{gauge sensitivity for gas}\} / \{\text{gauge sensitivity for argon}\}$ [15, 16].

	He	Ne	Ar	Xe	N ₂
r	0.13	0.20	1.00	2.29	0.84

As it can be seen in the Figure 4-5c, the adjusted Poisson curve for $k = 1$ fits the mass 36 signal rather well, suggesting that at this mass we indeed track the droplets that picked up one neon atom.

Signal at mass 40 rises more slowly and peaks at higher pressures than would be predicted by Poisson distribution for $k = 2$. In the same time, the distribution for $k = 3$ provides a good fit and peaks at the about the same pressure. This leads to a conclusion that mass 40 receives more contribution from droplets that picked up 3 or more argon atoms. Indeed, as indicated by Callicoatt and co-workers [5, 10], Ne₃ parent ion never survives the fragmentation, and its most likely fragment is Ne₂⁺. In the same time, they notice that large droplets ($\langle N \rangle = 3300$ helium atoms is the largest size reported in their study) containing 2 neon atoms tend to fragment into Ne₂He_n⁺ products. Helium droplets described in this dissertation are much larger ($\langle N \rangle \sim 8500$), so Ne₂He_n⁺ (and not Ne₂⁺) ions are even more likely to represent initially embedded Ne₂.

Argon

Similar to neon, we need to select the appropriate indicators of droplets that picked up a specific number of argon atoms. According to Callicoatt et al [5], ArHe_9^+ fragment results predominantly from ionization of droplets that carried one argon atom and Ar_2^+ signal comes from droplets that carried two. Ar_3^+ signal has been chosen as an indicator of droplets carrying three atoms of argon, however it also can appear as a result of fragmentation of a larger (Ar_n , $n \geq 4$) argon sub-clusters in the droplet. The pickup cell pressure dependence of these three signals, taken at masses 76, 80 and 120 respectively, is presented in Figure 4-6a. Note that the pressure scale is different from the case of neon. This is due to the fact that argon experiments were carried out with a different arrangement, in which the pressure gauge was located not in the pickup cell, but next to it in the experimental chamber (for overall layout schematics, see Ch. II). This resulted in systematically lower pressure readings. Consequently, it is impossible to simulate the pickup process employing the actual parameters of the apparatus. To correct for that, a scaling coefficient was introduced in the distribution. Its value has been varied to achieve the best fit for the Ar_2^+ pressure dependence. This signal receives very little contribution from droplets carrying dopants other than Ar_2 in this pressure range, and, therefore, its maximum is expected to accurately represent the maximum probability to pick up two argon atoms.

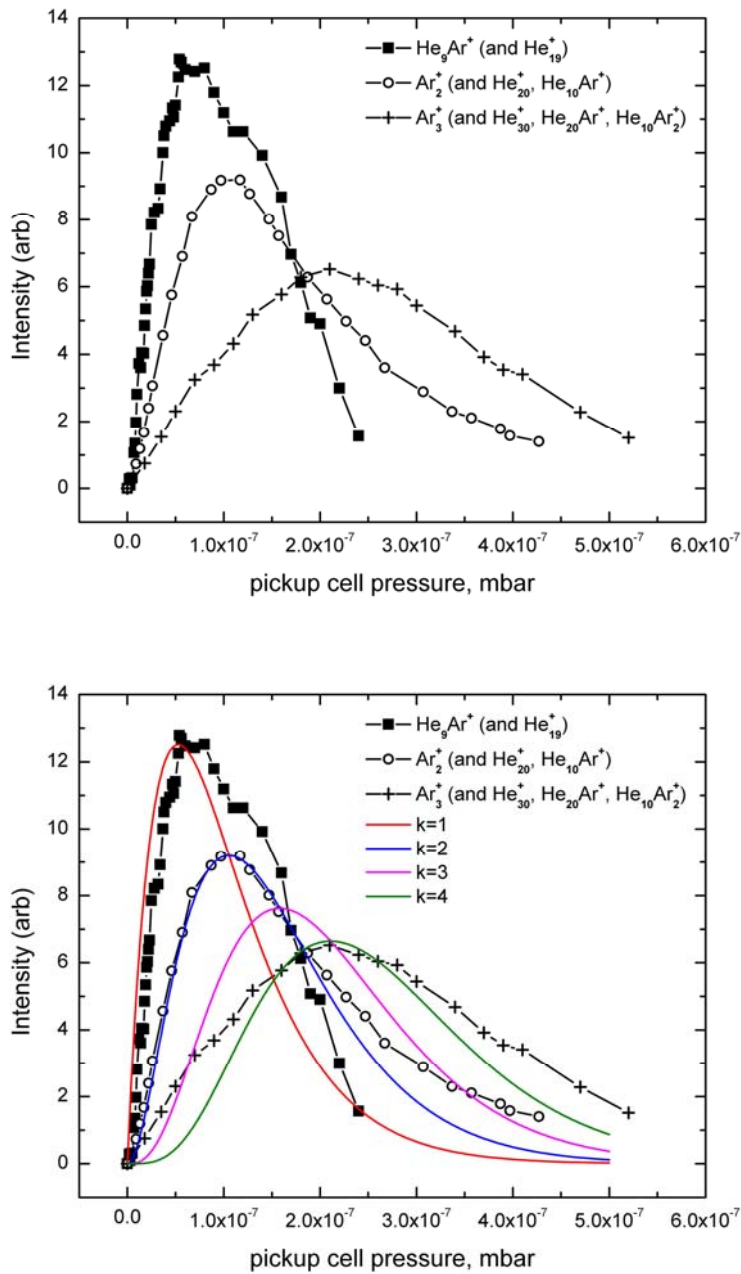


Figure 4.6. Calibration of argon pressure variation technique: a) pressure dependence of mass spectrometer signal at masses 76, 80 and 120; b) same as a) plus simulated probability distributions

The same parameter was used in the Poisson distributions for $k = 1, 3$ and 4 number of atoms. The results are shown in Figure 4-6b.

The simulated distribution for $k = 1$ fits the experimental data rather well, underestimating the peak probability pressure only slightly. This means that we can rely on this curve when adjusting the probability of picking up one argon atom.

The increase of mass 120 signal follows the $k = 3$ distribution at the very beginning, but then is better fit by the curve for $k = 4$, which also peaks at the same pressure. This suggests that this signal, which represents He_{30}^+ , ArHe_{20}^+ and $\text{Ar}_2\text{He}_{10}^+$, as well as Ar_3^+ , receives contribution from Ar_4 and larger argon sub-clusters.

Xenon

Measuring pressure dependence of fragmentation products of droplets containing xenon atoms was complicated by two factors:

- all five isotopes of xenon are present in comparable proportions in the mass spectrum
- resolution of our mass spectrometer is poor in the mass range above 100, becoming unacceptable above 200.

For these reasons it was impossible to monitor signals corresponding to Xe_n^+ for $n \geq 2$. Consequently, no data is available to represent droplets doped with two xenon

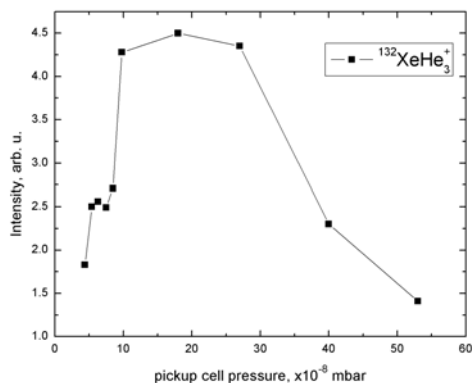


Figure 4- 7. Pickup cell pressure dependence of mass 144 signal.

atoms. Although Xe^+ is the most likely fragment of droplets carrying one xenon atom, droplets carrying 2 or more xenon atoms are also likely to yield this ion upon fragmentation. $^{132}\text{XeHe}_3^+$ was chosen as an indicator of singly doped droplets because a) this signal does not receive any significant contribution from droplets doped with more than one xenon atom, and b) it is a distinguishable peak in the mass spectrum. The pressure dependence of this signal, presented in Figure 4-7, shows a broad peak around $2 \cdot 10^{-8}$ mbar. The broadness and higher (than in the case of argon) peak pressure can be understood by taking into account the data from Table 4-2: the pressure scale for Xe differs from that of argon by a factor of ~ 2 . Hence, it was deemed reasonable to use these results when optimizing pickup probability of one xenon atom.

The overall results of this chapter can be concluded here as follows. Monitoring the pickup of foreign species by helium droplets is not straightforward. This is especially the case for noble gases, due to complex ionization and fragmentation processes. However, the obtained data and the calibrating simulations together constitute a reliable tool for selective doping of helium droplets with 1, 2 or 3 noble gas atoms. Hence, we are well equipped for studies of photo-initiated phenomena in NO₂-rare gas complexes, embedded in helium droplets.

References and Notes

1. B. E. Callicoatt, D. D. Mar, V. A. Apkarian, K. C. Janda, *J. Chem. Phys.* 105(17) (1996)
2. B. E. Callicoatt, K. Förde, L. F. Jung, T. Ruchti, K. C. Janda, *J. Chem. Phys.* 109(23) (1998)
3. K. R. Atkins, *Proceedings of International School of Physics Enrico Fermi, Course XXI on Liquid Helium*, edited by G. Careri (Academic, New York, 1963), pp. 403-413
4. N. Halberstadt, K. C. Janda, *Chem. Phys. Lett.* 282, 409-412 (1998)
5. B. E. Callicoatt, K. Förde, T. Ruchti, L. F. Jung, K. C. Janda, *J. Chem. Phys.* 108(22) (1998)
6. W. K. Lewis, C. M. Lindsay, R. J. Bemish, R. E. Miller, *J. Am. Chem. Soc.* 127, 7235 (2005)
7. A. M. Ellis, S. Yang, *Phys. Rev. A* 76 (2007)
8. T. Ruchti, B. E. Callicoatt, K. C. Janda, *Phys. Chem. Chem. Phys.* 2, 4075 (2000)
9. U. Hohm, K. Kerl, *Mol. Phys.* 69(5) (1990)
10. T. Ruchti, K. Förde, B. E. Callicoatt, H. Ludwigs, K. C. Janda, *J. Chem. Phys.* 109(24) (1998)
11. D. Bonhommeau, M. Lewerenz, N. Halberstadt, *J. Chem. Phys.* 128, 054302 (2008)
12. K. P. Huber and G. Herzberg, *Molecular Spectra and Molecular Structure, IV. Constants of Diatomic Molecules* (Van Nostrand Reinhold, New York, 1979), p. 300
13. C. E. Moore, *Atomic Energy Levels, NSRDS-NBS 35, Nat. Bur. Stand. US, Washington, DC, 1971, vol. 1-3*

14. C. Callegari, K. K. Lehmann, R. Schmied, G. Scoles, J. Chem. Phys., 115, 22 (2001)
15. S. Dushman, Scientific Foundations of Vacuum Technique, 2nd Ed., John Wiley & Sons, New York (1962), p.324, and references therein.
16. S. Dushman, A. H. Young, Phys. Rev., 68, 278 (1945)
17. Adjusting the scale of experimental data would be more correct, since this way it will correspond to the actual pressure. However, we will be using the same ion gauge in all experiments, so its “own” scale is more important for us as a tool.

V. Experimental Results

Extension of the Mass Depletion Spectrum to the Region of 17350–17750 cm^{-1}

The mass depletion spectra of NO_2 molecule embedded in helium droplets ($[\text{NO}_2]\cdot\text{DHe}$) in the interval of 17350–17750 cm^{-1} is presented in Figures 5-1 and 5-2. These results are the extension of the work by Polyakova *et al* [1] to the region of lower energies. It has been found that all of the key features of the spectrum, as described in Chapter III, remain the same at these excitation energies. The figures 5-1 and 5-2 also contain the stick spectrum from the LIF experiments by Jost and co-workers [2], as well as its convolution with lorentzian line shapes. It appeared that an average value of 6.5 cm^{-1} for widths provided a slightly better fit. This value is somewhat (albeit insignificantly) smaller than the line width of 7 cm^{-1} at the higher energies. This is consistent with the decreasing density of NO_2 eigenstates in this energy region. As described in Ch. 3, the total decay width for relaxation of the vibronic eigenstate is the sum of partial widths of all open decay channels, each channel being associated with lower-energy states of NO_2 . As the density of states decreases, the relaxation becomes less efficient and results in narrower lines. Closer to the bottom of the conical intersection, where the non-adiabatic coupling is less

strong density of states cannot be treated as continuous, and the approach of Ch. III would no longer be justified. Therefore, at lower energies it is reasonable to expect narrow lines and mode-specific shifts – characteristic of the regime of regular intramolecular dynamics [3].

Another feature of the obtained spectrum is the poor signal-to-noise ratio, which correlates with the smaller absorption cross-section of NO₂ at longer excitation wavelengths. Figure 5-3 shows the low-resolution spectrum of NO₂ molecule [4]. The energy interval investigated in the present experiment appears to be at the edge of the region where NO₂ absorbs well.

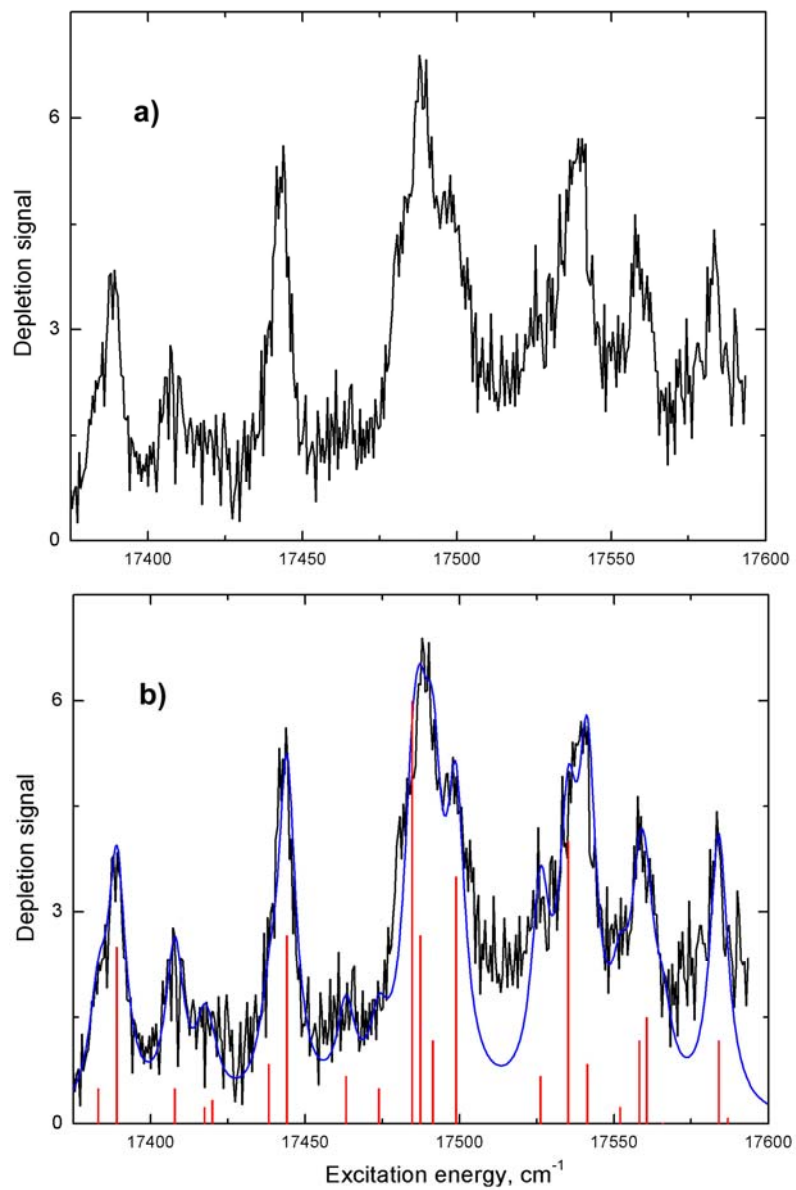


Figure 5-1. Mass depletion spectrum of NO₂ in helium droplets in the region 17350-17600 cm⁻¹. Panel a) shows the raw data; panel b) shows same spectrum, plus vibronic band origins from LIF experiment [2]. (red sticks) and its convolution with lorentzians of FWHM = 6.5 cm⁻¹ (blue line). Red sticks' heights correspond to LIF intensities.

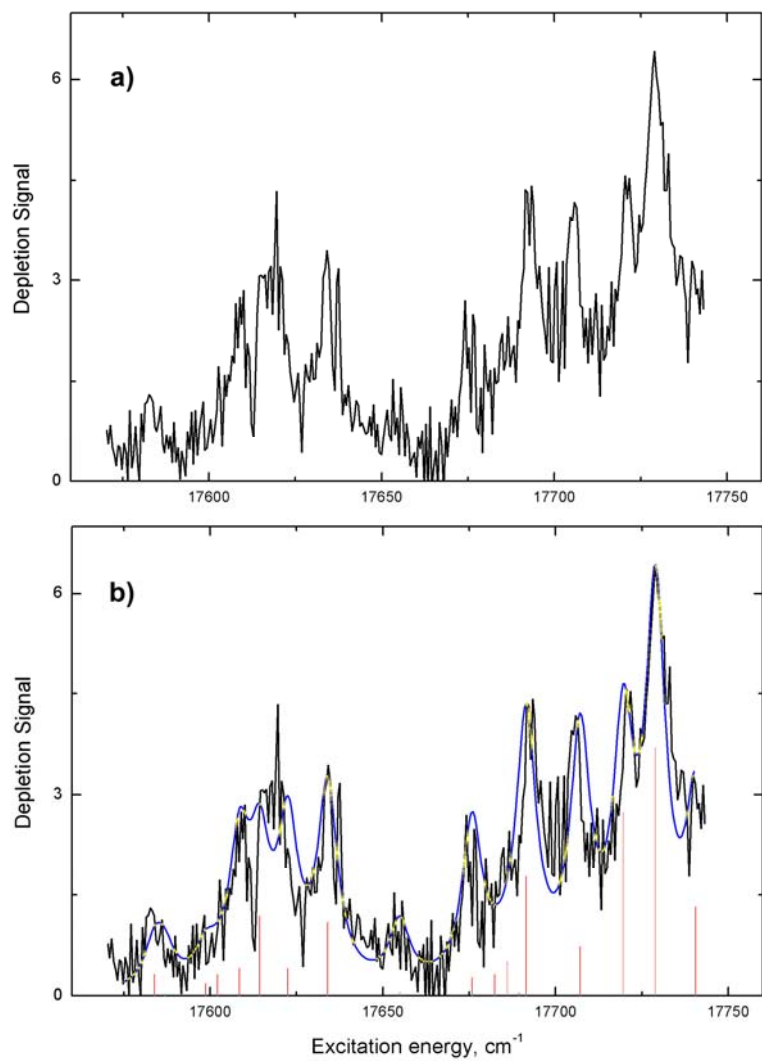


Figure 5-2. Same as in Figure 5-1 for the region 17550-17750 cm^{-1} .

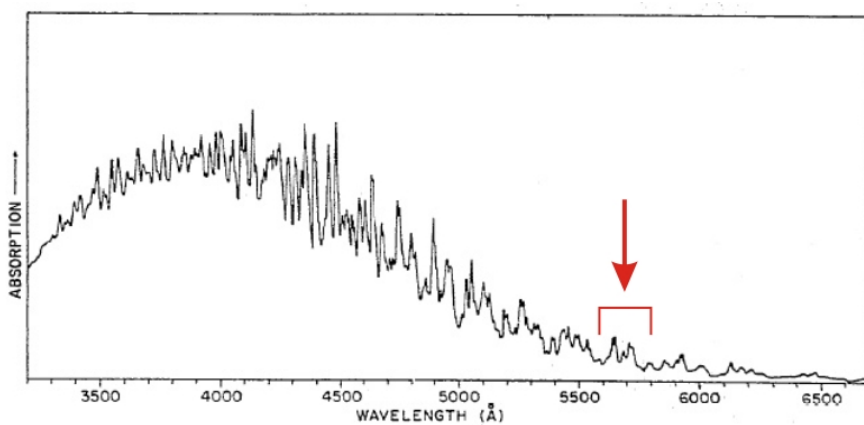


Figure 5-3. Low resolution absorption spectrum of NO₂ [4]. Arrow indicates the energy interval studied in this work.

Visible spectroscopy of NO₂-Rare Gas Complexes in Helium Droplets

Results

In this section the mass-depletion spectra of NO₂·RG (RG = Ne, Ar, Kr, Xe) complexes in helium droplets ([NO₂·RG]·DHe) are presented. The effect of addition of a rare gas atom was observed on two single isolated spectral lines of [NO₂]·DHe. In case of neon, krypton and xenon, the line at 17443 cm⁻¹ was monitored; for argon, both lines at 17443 cm⁻¹ and 17540 cm⁻¹ were monitored and no qualitative difference has been observed. Figure 5-4 indicates the locations of these lines in the spectrum.

Neon

The pronounced effect has only been observed in case of [NO₂·Ne]·DHe. It manifested itself as the decrease of the original line and the appearance of an additional broad spectral feature to the blue of the original line (see Figure 5-5). With increasing neon pressure the original line gradually disappeared and the additional feature became less intense. Due to poor signal-to-noise ratio it is impossible to characterize the additional feature with any certainty. However, the following can be safely asserted: a) the additional feature is due to the

[NO₂·Ne]·DHe, and b) it is broader and more blue-shifted than the original [NO₂]·DHe line.

Other rare gases

Figures 5-6, 5-7 and 5-8 demonstrate the effect of addition of argon, krypton and xenon, respectively. No additional features have been observed in these cases. The original [NO₂]·DHe spectral line gradually decreased with the pressure of the respective rare gas in the pickup cell. This decrease was faster upon addition of Kr and Xe, where the spectrum had been obliterated with pressure optimized for pickup of two gas atoms on average. The mechanisms responsible for these effects are discussed below.

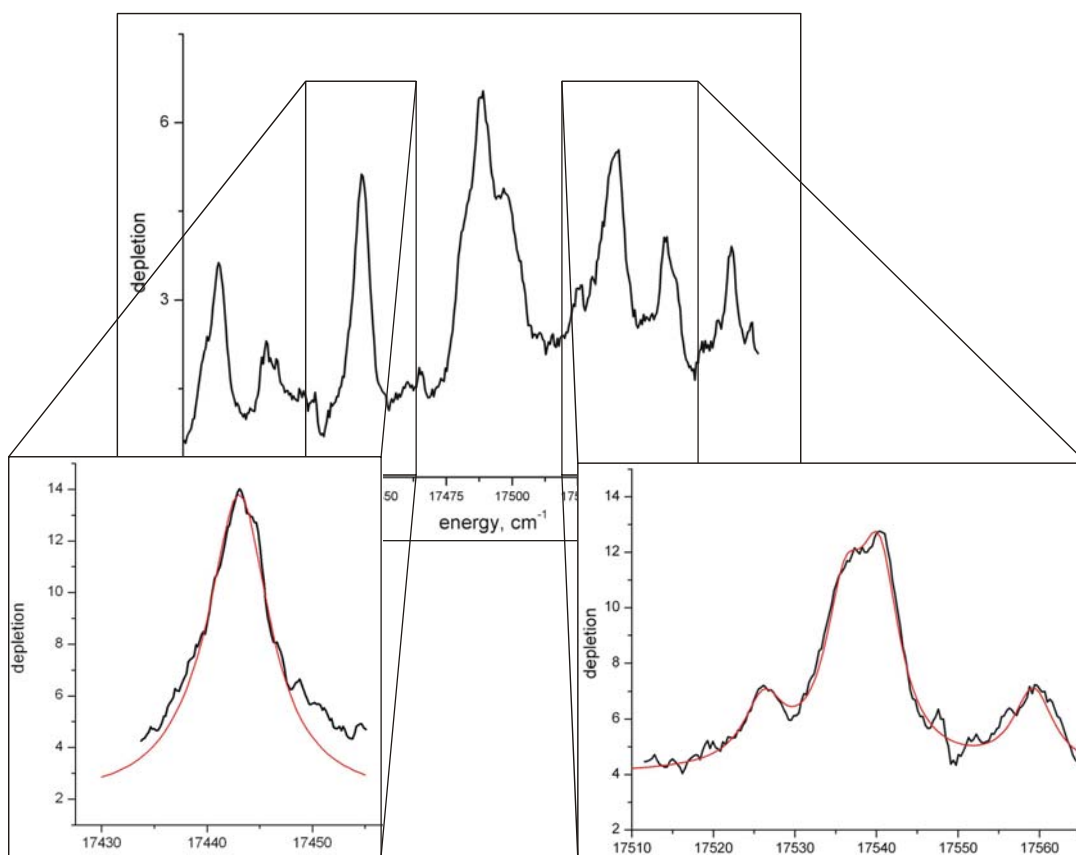


Figure 5-4. The two isolated lines of NO₂ spectrum on which the effect of rare gas addition was studied.

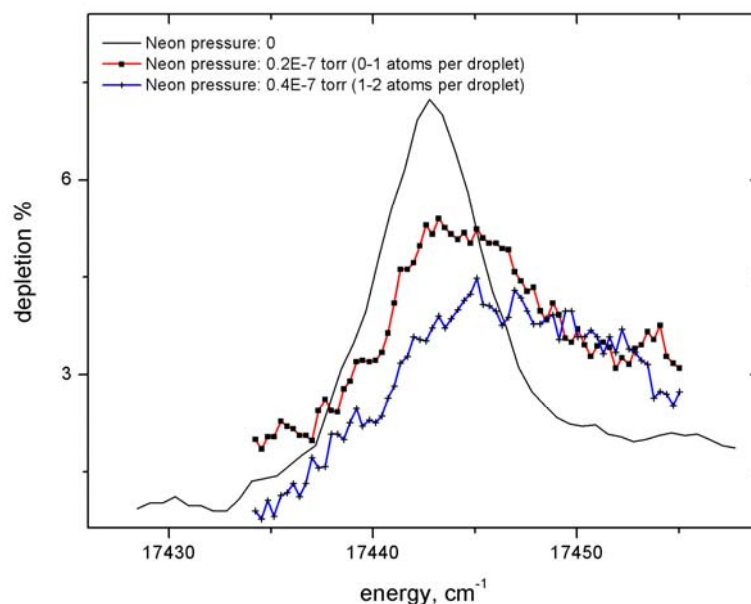


Figure 5-5. The effect on an isolated spectral line at 17443 cm^{-1} produced by addition of one (on average) neon atom to the droplets doped with NO_2 .

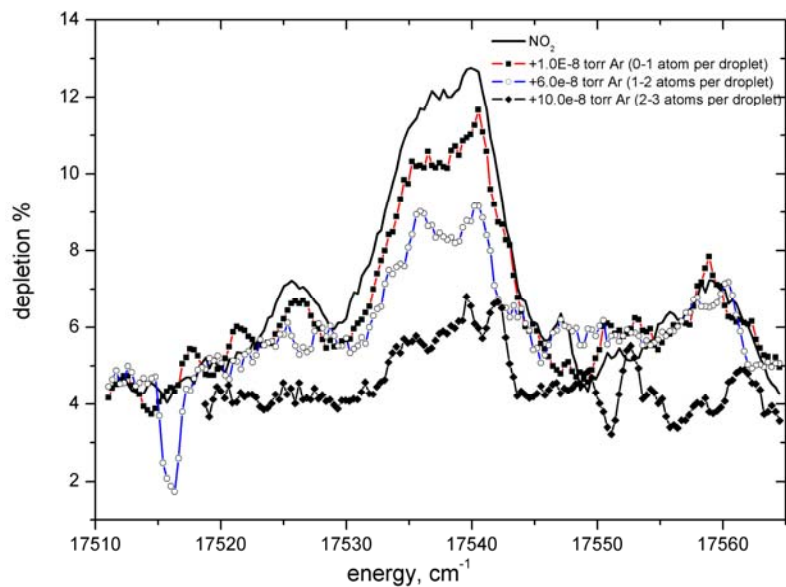


Figure 5-6. The effect on an isolated spectral line at 17540 cm^{-1} produced by addition of argon atoms to the droplets doped with NO_2 .

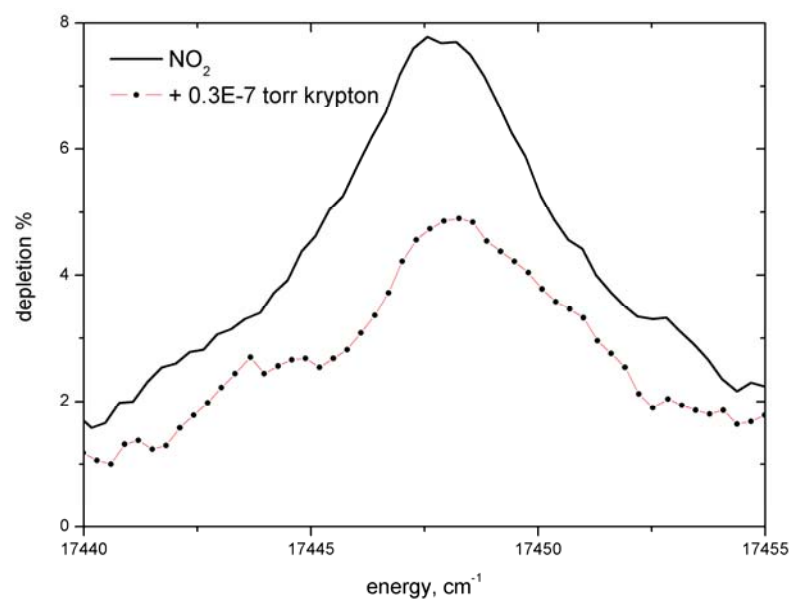


Figure 5-7. Same as 5-4 for krypton.

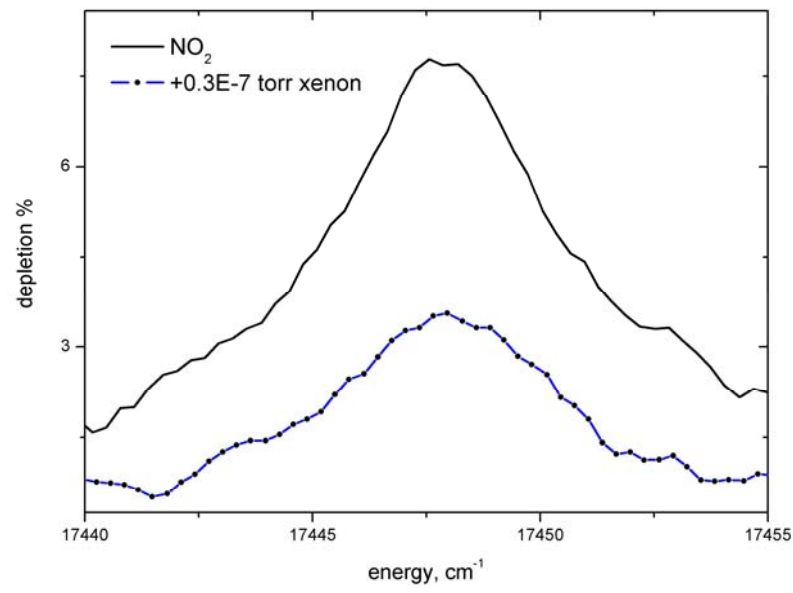


Figure 5-8. Same as 5-4 for xenon.

Discussion

Neon

The perturbation brought about by neon is minor, as evidenced by only modest additional shift and broadening. There is no qualitative change in the guest-host interaction, *i.e.* the separation of couplings and timescales described in Ch. III holds. Neon atom displaces one of the helium atoms in the closest shell and slightly changes the non-superfluid structure around the NO₂ chromophore. Therefore, additional feature in the spectrum of [NO₂·Ne]·DHe can be explained as inhomogeneous broadening of the gas-phase NO₂ spectral line due to multiple configurations of the non-superfluid medium around the molecule.

Consider the structure of NO₂·Ne complex. Although no data is available for this particular complex in the gas phase, it is reasonable to expect a configuration similar to the one in Figure 5-9. The gas phase complexes of NO₂·RG (RG = Ar, Kr) had been found to be rather floppy by Howard and co-workers [5], with almost free rotation of NO₂ about its prolate axis. Gas phase NO₂·Ne would be expected to have similar structure and intermolecular behavior. Inside the helium droplet, formation of NO₂·Ne would not necessarily follow the lowest energy path due to extremely cold environment. This may lead to different structural isomers of the complex. Moreover, since neon atoms in helium are surrounded by a shell of helium atoms, there would be structural isomer of the non-superfluid medium around the NO₂·Ne complex. The density of helium around neon, $\sim 0.04 \text{ \AA}$, is

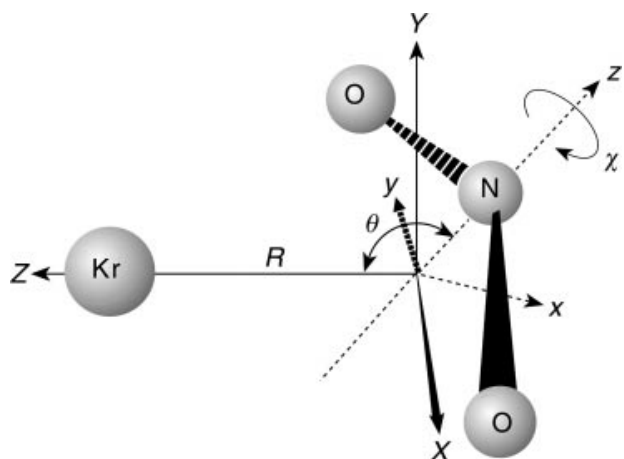


Figure 5-9. Geometry of $\text{NO}_2\cdot\text{Kr}$ complex, from Howard *et al* [5b]. The reference axes (x,y,z) correspond precisely to the principal inertial axes of NO_2 (c,a,b) , and the axes (X,Y,Z) correspond approximately to the inertial axes (B,C,A) of the complex.

somewhat smaller, but comparable to that of NO_2 , ~ 0.08 [6]. Each of the possible $[\text{NO}_2\cdot\text{Ne}]\cdot\text{DHe}$ shell structures will induce its own shift and broadening of the spectrum.

As the pickup cell pressure is increased, more neon atoms coagulate around NO_2 . Unfortunately, in the present experiment it was impossible to establish the pickup sequence of NO_2 and neon, since both gases were simultaneously added to the same pickup cell. However, unlike Ar clusters [7], neon may remain fluxional in helium droplets at 0.37 K. Recent findings of Eloranta [8], who suggested the formation of crystalline gel structure, seem like a supporting argument in this case. This may lead to NO_2 being preferably surrounded by neon atoms, rather than being on the surface of the preformed neon cluster, regardless of the pickup sequence.

This fact increases the number of structural isomers in the droplet beam which may contribute to further inhomogeneous broadening.

The size distribution of neon clusters becomes larger with pressure in the pickup cell. It is about $\pm\sqrt{N}$ due to Poisson pickup statistics, and may be additional source of inhomogeneous broadening.

Other rare gases

The general behavior observed in the spectra upon addition of rare gas atoms is the decrease of intensity of the spectral line. This can be explained by overall decrease of the mass spectrometer signal at certain m/z , which results from changing droplet fragmentation patterns after electron-impact ionization.

All measurements reported here were recorded by observing signal at $m/z = 30$, which corresponds to NO^+ . The ability to infer information about laser induced processes that occurred in a given droplet depends on the chance of this droplet to produce NO^+ fragment after ionization. Figure 5-10 shows the major categories of droplets that are present in the beam, when pickup cell is filled only with NO_2 gas and the pressure is optimized for pickup of one NO_2 molecule on average. The sizes of “droplets” in the figure reflect the relative abundances in the beam. The arrows indicate possible ionization fragments. For each category, fragmentation results in a distribution of ion products, one of which may or may not be NO^+ . The broader the distribution (= the larger the number of possible “Other Products” on the left side) –

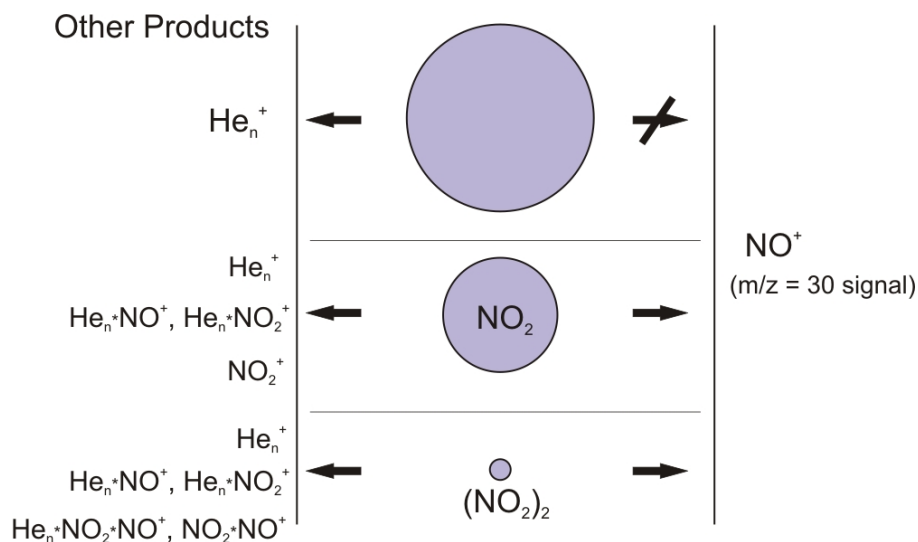


Figure 5-10. Schematic distribution of fragmentation products upon electron-impact ionization for the beam of droplets doped with NO_2 . NO_2 pressure in the pickup cell is optimized for pickup of one molecule on average.

the less likely is the droplet to produce NO^+ fragment. This likelihood times the abundance determines the overall contribution to the $m/z = 30$ signal on the mass spectrometer.

Figure 5-11 shows the categories of droplets in the beam when rare gas is added to the pickup cell and its pressure is optimized for pickup of one atom on average. Since the overall number of droplets remains the same, categories from Fig. 5-10 are now split. The number of droplets carrying just single NO_2 molecule (this category is the major contributor to the $m/z = 30$ signal) is significantly reduced. For the new categories, such as droplets doped with $\text{NO}_2 \cdot \text{RG}$, $\text{NO}_2 \cdot (\text{RG})_2$, *etc*, the distribution on the left side is broad, hence the probability to form NO^+ is

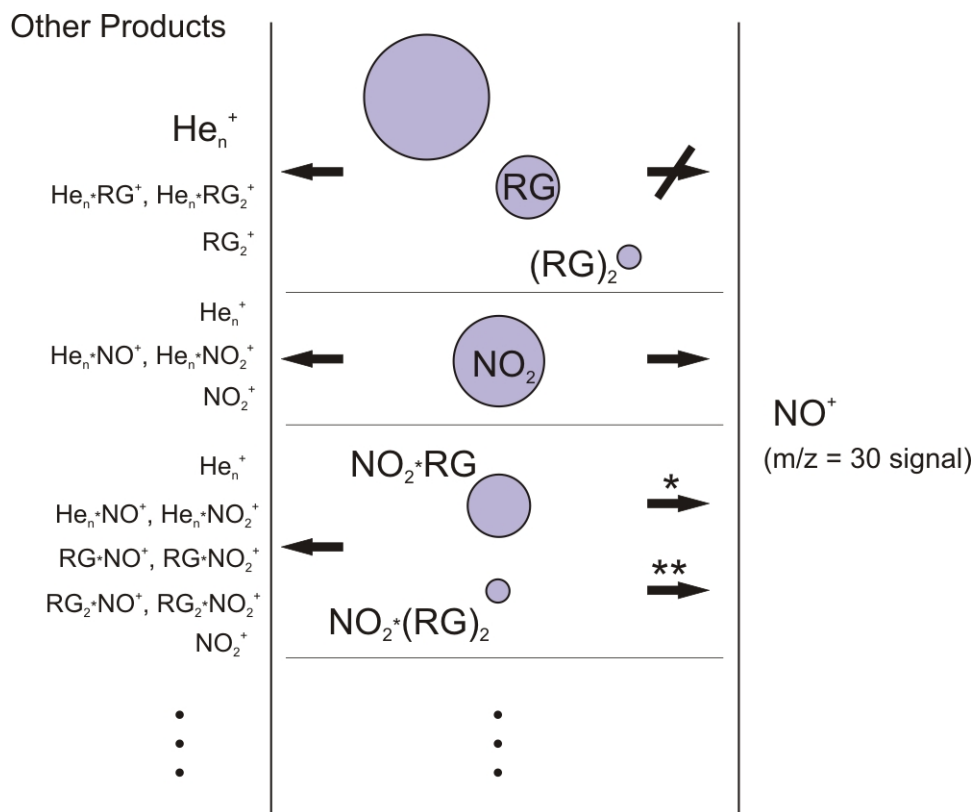


Figure 5-11. Schematic distribution of fragmentation products upon electron-impact ionization for the beam of droplets doped with NO_2 and rare gas atoms ($\text{RG} = \text{Ne}, \text{Ar}, \text{Kr}$ and Xe). NO_2 pressure - same as in Fig. 5-8, RG pressure is optimized for pickup of one atom on average.

smaller. Therefore, comparing the diagrams in Figures 5-10 and 5-11 explains the general shrinkage of the $m/z = 30$ peak in the mass spectrum with addition of a rare gas to the pickup cell. Consequently, the intensity of any laser-induced signal, observed on this m/z peak, will decrease as well.

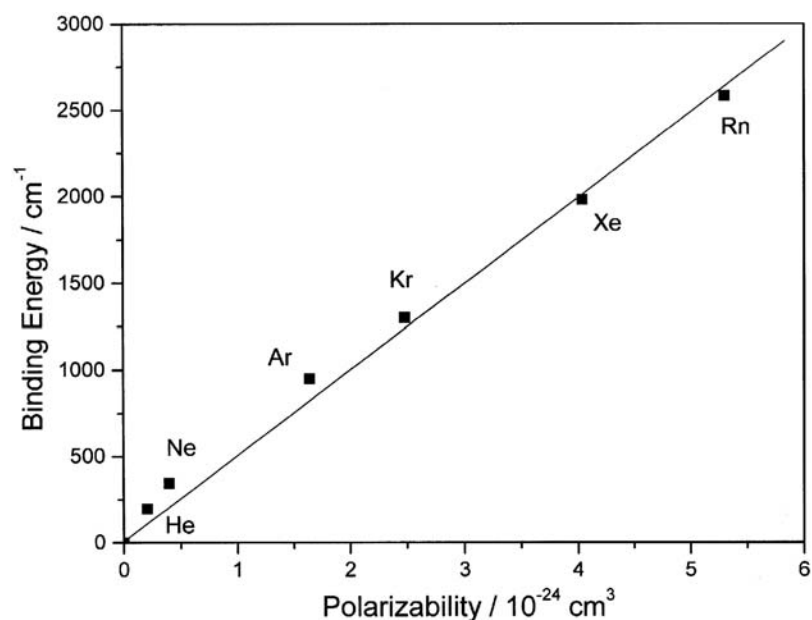


Figure 5-12. RG·NO⁺ binding energy vs. polarizability, RG = He – Rn [9].

However, the situation can be qualitatively different for different rare gases. Based on observations of the neon-induced effect discussed above, it can be said that processes indicated as (*) and (**) in Figure 5-11 are significant enough to convey the spectroscopic information in case of addition of neon atoms.

The “Other Products” list is the same in case of RG = Ar, Kr or Xe. However, the probability distribution among those products may be substantially different due to stronger binding of these species to NO₂ and NO⁺. In other words, stronger interaction can “cross out” the arrows marked (*) and (**). In this case, the only contribution to the NO⁺ signal will come from “single NO₂ molecule” droplets, the number of which goes down with RG pressure. This could explain the absence of additional features and decrease in the overall intensity in the spectra in Figures

5-6, 5-7 and 5-8. Figure 5-12 illustrates the binding energies of NO^+ cation to rare gas atoms [9]. It is apparent that there is a large difference in binding energy when going from Ne to other rare gases.

There is, however, difference between the spectrum in Figure 5-6 (argon) and spectra in Figures 5-7 and 5-8 (krypton and xenon, respectively). The difference is the baseline. The mechanism of signal decrease discussed above would quickly bring the baseline to zero – all light-absorbing droplets will show up at mass signals other than $m/z = 30$. The baseline in Figure 5-6 goes down much slower than in 5-7 and 5-8, decreasing significantly only when 2-3 argon atoms on average are present in the droplet. First of all, this suggests that processes such as those marked with (*) in the Figure 5-11 still occur with appreciable efficiency. It means that there could be an alternative reason for absence of spectroscopic features – the changes in NO_2 relaxation dynamics brought about by argon. Namely, the processes discussed above for the case of Ne could take place in case of Ar as well, but to much greater extent due to stronger $\text{NO}_2\cdot\text{Ar}$ interaction. This interaction could obliterate spectral features, leaving only broad absorption baseline.

The only way determine if this is the observed effect is to investigate the mass-depletion behavior at other m/z signal – the ones corresponding to more probable fragmentation products. The best candidates would be $\text{RG}\cdot\text{NO}^+$ and $\text{RG}\cdot\text{NO}_2^+$. The question is which one would give better signal, and the answer lies

in the ability of the rare gas atom to affect the post-ionization fragmentation of NO_2 molecule. It is known that extensive fragmentation of fragile organic molecules, which ensues after ionization in helium droplets, can be suppressed by co-embedding water molecules [10]. Kresin and co-workers argue that larger dipole moment of water may divert the charge transfer toward this molecule, although it may have a larger ionization potential. The ultimate ionization of the organic molecule occurs via charge transfer from water rather than from He^+ , which leaves much less extra energy available for fragmentation. However, this would hardly be the case for co-embedding with rare gas atoms, since NO_2 will always be the primary target for the migrating charge. It is also unlikely that a rare gas atom will somehow affect the fragmentation of the nascent NO_2^+ ion. The energy available at the moment of charge transfer from He^+ (24.6 eV) prepares NO_2^+ in one of the highly excited electronic states, which couple efficiently to the dissociative continua through a number of $\{\text{NO}^+ + \text{O}\}$ repulsive curves [11,12]. This coupling is robust and is not likely to be compromised by the presence of a rare gas atom. Therefore, it seems reasonable to expect the products of the NO_2 post-ionization fragmentation to be essentially the same as in the gas phase, as well as in helium droplets, with NO^+ being the most likely fragment. Hence, the $\text{RG}\cdot\text{NO}^+$ mass peak should be the first to look for depletion signal. Of course, He_2^+ fragments at $m/z = 8$ always carry the depletion information, however, to a lesser extent due to contributions from non-

depleting droplets. Poor signal-to-noise ratios have prevented the observation of spectra at this m/z signal

In the context of obliteration of spectral features of NO_2 by the presence of rare gas atoms it is worth to mention the studies of NO_2 in solid rare gas matrices. This has been studied by Resonance Raman [13] and visible absorption spectroscopy [14, 15]. $A^2B_2 \leftarrow X^2A_1$ absorption spectrum of NO_2 in all matrices shows broad unresolved lines of FWHM $\sim 30 - 150 \text{ cm}^{-1}$. Although it is unlikely to expect exact solid-like behavior from rare gas aggregates in helium droplets, broadening of 30 cm^{-1} induced by a rigid cluster could already prevent the observation of any features in the present experiment.

References and Notes

1. E. Polyakova, D. Stolyarov, X. Zhang, V. V. Kresin, C. Wittig, *Chem. Phys. Lett.* 375(3-4), 253 (2003)
2. R. Georges, A. Delon, R. Jost, *J. Chem. Phys.* 103(5), 1732 (1995)
3. F. Madeja, P. Markwick, M. Havenith, K. Nauta, R. E. Miller, *J. Chem. Phys.* 116(7), 2870 (2002); see also J. P. Toennies, A. Vilesov, *Angew. Chem. Int. Ed.* 43, 2622 (2004) for review.
4. D. K. Hsu, D. L. Monts, R. N. Zare, *Spectral Atlas of Nitrogen Dioxide, 5530 to 6480 Å*, Academic Press, New York (1978)
5. a) R. J. Low, M. D. Brookes, C. J. Whitham, B. J. Howard, *J. Chem. Phys.* 105(16), (1996); b) S. Blanco, C. J. Whitham, H. Qian, B. J. Howard, *Phys. Chem. Chem. Phys.* 3, 3895 (2001)
6. F. Dalfovo, *Z. Phys. D* 29, 61 (1994)
7. S. Kuma, H. Goto, M. N. Slipchenko, A. F. Vilesov, A. Khramov, T. Momose, *J. Chem. Phys.* 127, 214301 (2007)
8. J. Eloranta, *Phys. Rev. B* 77, 134301 (2008)
9. E. P. F. Lee, P. Soldan, T. G. Wright, *J. Phys. Chem. A*, 102 (34), 6858 (1998)
10. Y. Ren, V. V. Kresin, *J. Chem. Phys.* 128, 074303 (2008)
11. C. R. Brundle, D. Neumann, W. C. Price, D. Evans, A. W. Potts, D. G. Streets, *J. Chem. Phys.* 53(2), 705 (1970)
12. H. Chang, M. Huang, *ChemPhysChem* 10, 582 (2009)
13. F. Bolduan, H. J. Jodl, *J. Mol. Spec.* 91, 404 (1982)
14. H. D. Bist, J. C. D. Brand, A. R. Hoy, V. T. Jones, R. J. Pirkle, *J. Mol. Spec.* 66, 411 (1977)
15. F. Bolduan, H. J. Jodl, *J. Mol. Struct.* 116, 361 (1984)

VI. Future Work

Signal-to-noise ratio

One of the paramount goals to be pursued during the course of further experiments is the improvement of signal-to-noise (S/N) ratio. Good quality data would enable detailed characterization of the additional feature in the spectrum of [NO₂·Ne]·DHe, described in the previous chapter. High S/N would also permit the observation of depletion signal at $m/z = 8$ peak (He₂⁺), which may elucidate the ambiguities related to changing product ion distributions.

Two major factors determine the good signal-to-noise ratio: i) high quality of the droplet beam, and ii) well-performing mass spectrometer. The issue of poor beam quality is best addressed by fixed attachment of cryogenic nozzle to the cold head, similar to the construction utilized by the group of Prof. A. Vilesov [1]. This way it can be assured that droplet beam enters the experimental chamber along the principal axis of the machine. With the current setup, described in Chapter II, helium expansion direction is sometimes hard to control.

A brand new mass spectrometer could solve the problem of instability and low S/N of the current one. Unfortunately, frequent and often unpredictable failures of the 1973 quadrupole mass spectrometer by Balzers prevented many measurements from being done systematically.

Monitoring $NO^+ \cdot RG$ and $NO_2^+ \cdot RG$ m/z peaks

As mentioned in the previous chapter, a search for the depletion information at other m/z peaks seems very promising. Mass depletion spectra recorded at peaks corresponding to $NO^+ \cdot RG$ and $NO_2^+ \cdot RG$ ($RG = Ar, Kr, \text{ and } Xe$) could reveal features that are not observed at $m/z = 30$ (NO^+). Further on, evolution of these signals with pressure in the pickup cell would provide clues on rare gas cluster formation around NO_2 .

Fluorescence of $NO_2 \cdot RG_N$ complexes in helium droplets

Finally, fluorescence of nitrogen dioxide in rare gas matrices [2] suggests an interesting experiment looking into rare gas atoms coagulation dynamics around NO_2 in helium droplets. In principle, simultaneous mass depletion and LIF studies are possible with the current experimental setup. The only major modification to the helium machine would be the addition of a second pickup cell to establish a certain pickup sequence. Observing the onset of fluorescence at certain pressures of rare gas in the second cell would shed light on structure and dynamics of the rare gas aggregates in the droplets. The results could then be readily compared to solid-state properties of rare gas matrices [3], or to the recently proposed “quantum gel” crystalline structure [4].

References and notes

1. M. Slipchenko, *Vibronic and Rovibrational Spectroscopy of Molecules and Molecular Clusters in Helium Nanodroplets*, PhD Thesis, University of Southern California (2005)
2. F. Bolduan, H. J. Jodl, *J. Mol. Spec.* 91, 404 (1982)
3. L. Andrews, M. Moskovits, *Chemistry and Physics of Matrix Isolated Species*, North-Holland, Amsterdam (1989)
4. J. Eloranta, *Phys. Rev. B* 77, 134301 (2008)

Appendix A. Depletion percentage calculation

The procedure below describes the way to quantify the depletion of a helium droplet beam, when the detector signal is proportional to the ionization probability of the droplet, rather than the absolute mass.

1. Suppose that a “train” of N doped droplets arrives at the mass spectrometer ionizer region. The probability to ionize one such droplet is A .

2. The signal S on the mass spectrometer receives a contribution of 1 if the droplet is ionized and 0 otherwise.

3. The probability $P_{S=N}^A$ that $S = N$ after the arrival of the “train” is

$$P_{S=N}^A = A^N . \text{ And, [1]}$$

$$P_{S=N-1}^A = (1 - A) \cdot A^{N-1} \cdot N$$

$$P_{S=N-2}^A = (1 - A)^2 \cdot A^{N-2} \cdot \frac{N(N-1)}{2}$$

...

$$P_{S=N-k}^A = (1 - A)^k \cdot A^{N-k} \cdot \frac{N(N-1) \cdots (N-k+1)}{k!} \tag{A1}$$

or

$$P_{S=k}^A = A^k (1 - A)^{N-k} \cdot C_N^k$$

4. When observing such “trains” continuously, the average mass spectrometer signal is

$$\bar{S} = \sum_{k=0}^N k \cdot P_{S=k}^A \quad (\text{A2})$$

5. When the laser is turned on, each “train” contains X droplets which shrunk due to the absorption of a photon. The probability to ionize one such droplet is B . Now the mass spectrometer signal receives two contributions from the two kinds of droplets:

$$\bar{S1} = \sum_{k=0}^{N-X} k \cdot P_{S=k}^A, \quad (\text{A3})$$

and

$$\bar{S2} = \sum_{k=0}^X k \cdot P_{S=k}^B \quad (\text{A4})$$

The observed depletion is:

$$D = \frac{\bar{S} - (\bar{S1} + \bar{S2})}{\bar{S}} \quad (\text{A5})$$

6. To determine the fraction of droplets that absorbed laser radiation, knowledge of the following is needed: the average droplet size, how the ionization probability varies with droplet size, and the observed depletion %. In this case, the average droplet size is 8500 atoms; the probability varies as $N^{2/3}$ (where N – number of atoms); the depletion is 10%. These conditions determine the parameters: $A=1$, $B=0.7$, $D=0.1$. Now Eq. (A5) can be solved for the fraction of interest X/N . Thus it is shown that less than a third of all droplets absorb radiation.

References and Notes

1. This is similar to consecutively pulling out N balls out of a bin, which contains black and white balls. Probability to pull out a black ball is A , white one $-(1-A)$. Only black balls count ($=S$). For derivation, see any textbook on probability and statistics, for example E. Parzen, *Modern Probability Theory and its Applications*, New York: Wiley, (1960)